



Since January 2020 Elsevier has created a COVID-19 resource centre with free information in English and Mandarin on the novel coronavirus COVID-19. The COVID-19 resource centre is hosted on Elsevier Connect, the company's public news and information website.

Elsevier hereby grants permission to make all its COVID-19-related research that is available on the COVID-19 resource centre - including this research content - immediately available in PubMed Central and other publicly funded repositories, such as the WHO COVID database with rights for unrestricted research re-use and analyses in any form or by any means with acknowledgement of the original source. These permissions are granted for free by Elsevier for as long as the COVID-19 resource centre remains active.



FDA approved drugs with antiviral activity against SARS-CoV-2: From structure-based repurposing to host-specific mechanisms

Mahmoud S. Ahmed^{a,j,*}, Ayman B. Farag^{a,1,2}, Ian N. Boys^{b,1}, Ping Wang^{a,1}, Ivan Menendez-Montes^a, Ngoc Uyen Nhi Nguyen^a, Jennifer L. Eitson^b, Maikke B. Ohlson^b, Wenchun Fan^b, Matthew B. McDougal^b, Katrina Mar^b, Suwannee Thet^a, Francisco Ortiz^f, Soo Young Kim^a, Ashley Solmonson^h, Noelle S. Williams^f, Andrew Lemoff^g, Ralph J. DeBerardinis^{h,i}, John W. Schoggins^{b,**}, Hesham A. Sadek^{a,c,d,e,*}

^a Department of Internal Medicine, University of Texas Southwestern Medical Center, Dallas, TX 75390, USA

^b Department of Microbiology, University of Texas Southwestern Medical Center, Dallas, TX 75390, USA

^c Department of Molecular Biology, University of Texas Southwestern Medical Center, Dallas, TX 75390, USA

^d Department of Biophysics, University of Texas Southwestern Medical Center, Dallas, TX 75390, USA

^e Center for Regenerative Science and Medicine, University of Texas Southwestern Medical Center, Dallas, TX 75390, USA

^f Department of Pharmacology, University of Texas Southwestern Medical Center, Dallas, TX 75390, USA

^g Department Biochemistry, University of Texas Southwestern Medical Center, Dallas, TX 75390, USA

^h Children's Medical Center Research Institute, University of Texas Southwestern Medical Center, Dallas, TX 75390, USA

ⁱ Howard Hughes Medical Institute, University of Texas Southwestern Medical Center, Dallas, TX 75390, USA

^j Department of Pharmaceutical Sciences, Jerry H. Hodge School of Pharmacy, Texas Tech University Health Sciences Center, Amarillo, TX, 79106, USA

ARTICLE INFO

Keywords:

SARS-CoV-2

Structure-based drug repurposing

Purine Metabolism

ABSTRACT

The continuing heavy toll of the COVID-19 pandemic necessitates development of therapeutic options. We adopted structure-based drug repurposing to screen FDA-approved drugs for inhibitory effects against main protease enzyme (Mpro) substrate-binding pocket of SARS-CoV-2 for non-covalent and covalent binding. Top candidates were screened against infectious SARS-CoV-2 in a cell-based viral replication assay. Promising candidates included atovaquone, mebendazole, ouabain, dronedarone, and entacapone, although atovaquone and mebendazole were the only two candidates with IC50s that fall within their therapeutic plasma concentration. Additionally, we performed Mpro assays on the top hits, which demonstrated inhibition of Mpro by dronedarone (IC50 18 μ M), mebendazole (IC50 19 μ M) and entacapone (IC50 9 μ M). Atovaquone showed only modest Mpro inhibition, and thus we explored other potential mechanisms. Although atovaquone is Dihydroorotate dehydrogenase (DHODH) inhibitor, we did not observe inhibition of DHODH at the respective SARS-CoV-2 IC50. Metabolomic profiling of atovaquone treated cells showed dysregulation of purine metabolism pathway metabolite, where ecto-5'-nucleotidase (NT5E) was downregulated by atovaquone at concentrations equivalent to its antiviral IC50. Atovaquone and mebendazole are promising candidates with SARS-CoV-2 antiviral activity. While mebendazole does appear to target Mpro, atovaquone may inhibit SARS-CoV-2 viral replication by targeting host purine metabolism.

* Correspondence to: Departments of Microbiology and Internal medicine/Division of Cardiology, University of Texas Southwestern Medical Center, 6000 Harry Hines Blvd, Dallas, TX 75390, USA.

** Corresponding author.

E-mail addresses: Mahmoudsalama.ahmed@ttuhsc.edu, Mahmoud.ahmed@utsouthwestern.edu (M.S. Ahmed), john.schoggins@utsouthwestern.edu (J.W. Schoggins), hesham.sadek@utsouthwestern.edu (H.A. Sadek).

¹ Authors contributed equally

² Author is currently at Department of Pharmaceutical Chemistry, Faculty of Pharmacy, Ahran Canadian University, 6th of October City, Giza, Egypt

<https://doi.org/10.1016/j.bioph.2023.114614>

Received 10 February 2023; Received in revised form 20 March 2023; Accepted 26 March 2023

Available online 28 March 2023

0753-3322/© 2023 The Authors. Published by Elsevier Masson SAS. This is an open access article under the CC BY license (<http://creativecommons.org/licenses/by/4.0/>).

1. Introduction

SARS-CoV-2 was identified in late December 2019 as the etiological agent of a severe acute respiratory disease named COVID-19 [1–3]. The virus has since propagated worldwide, causing an unprecedented incidence of morbidity and mortality. The unprecedented efforts by the scientific community yielded a number of highly effective therapeutics, including orally available antiviral agents approved by the U.S. Food and Drug Administration, such as; Paxlovid (nirmatrelvir tablets and ritonavir tablets) for the treatment of mild-to-moderate coronavirus disease (COVID-19) in adults and pediatric patients [4,5]. However, despite its effectiveness, the use may be limited by compliance issues, and a number of interactions with several drugs that can lead to serious adverse effects [6]. Importantly, COVID-19 vaccines may not offer complete protection due to the rapid and continuous mutations shown by the virus [7,8]. Drug-repurposing strategies provided a path towards identifying potential therapeutics that have established safety profiles and that can be used individually or in combination for targeting viral proteins or host factors required for viral replication [9–12]. To date, several strategies to identify and possibly repurpose drugs for SARS-CoV-2 have been reported including but not limited to remdesivir, favipiravir, tocilizumab, and baricitinib [11,13–21]. SARS-CoV-2 is a beta coronavirus and its genome encode several structural proteins, including the glycosylated spike (S) protein that mediates viral attachment to the cells by binding to angiotensin-converting enzyme 2 (ACE2), a membrane bound carboxypeptidase [22–24]. Viral entry also appears to be mediated by priming of S protein facilitated by the host cell-produced serine protease TMPRSS2 [22,25]. In addition, the viral genome also encodes nonstructural proteins including an RNA-dependent RNA polymerase (RdRp), main protease (Mpro), and papain-like protease (PLpro) [26–28]. Therefore, targeting ACE2, TMPRSS2, RdRp, Mpro, and PLpro as individual targets, or in combination created viable strategies for repurposed drugs.

A number of these viral proteins have been studied intensively from structural and medicinal chemistry perspectives owing to their potential role as therapeutic targets [29,30] but perhaps Mpro has been one of the most intensely studied SARS-CoV-2 proteins. Mpro, a 33.8-kDa 3 C-like protease, is responsible for proteolytic cleavage of the viral polyproteins pp1a and pp1b, which is required for viral replication and transcription. Mpro cleaves proteins at conserved sequences typically following a sequence that includes the amino acid glutamine, and has no homology to human proteases, which makes it an attractive drug target. One of the earliest structural publications on Mpro was an elegant study which solved the crystal structure of Mpro in complex with an inhibitory peptide N3 (PDB ID: 6LU7). Notably, the inhibitory peptide binds the substrate-binding pocket of SARS-CoV-2 Mpro. Thus, we were one of the first initiative research groups that used this domain as the focus of an *in-silico* screen to identify FDA approved drugs with activity against Mpro, coupled with *in vitro* assays [31]. However, the viral inhibition profiles were not well correlated with Mpro inhibitory profiles for our selected drugs. Therefore, we decided to investigate the mechanism outlining the antiviral activity for the selected drugs.

2. Results

The structural analysis for the peptide ligand N3 co-crystallized with SARS-CoV-2 Mpro substrate-binding pocket revealed a significant number of hydrophobic interactions and a hydrogen bond network comprising His163, His164, Glu166, Gln189, and Thr190 [32]. We decided to conduct an *in silico* molecular modeling study for > 2000 FDA approved drugs focusing on two potential sites of the Mpro substrate-binding pocket based on the co-crystallized peptide N3.

Central site molecular docking: The central site docking results showed the top 11 hits based on their S score, binding affinity, interacting amino acids, and binding mode to fit the main protease pocket with respect to the reported clinical indication, as shown in Table 1. The

rest of the top hits are listed in Table S1. Our three and two-dimensional analyses for the top hits are shown in Fig. 1 and Fig. S1. Darunavir, a known antiviral protease inhibitor [33], showed the best binding affinity in terms of hydrophobic-hydrophobic and hydrogen bond interactions with His163, Glu166, and Thr190 at S score – 14.03040 Kcal/mol. The top candidates also included antivirals such as Nelfinavir and Saquinavir with S scores ranging from – 13.4200 Kcal/mol to – 12.0917 Kcal/mol. The current repurposing study also includes other drugs approved for different clinical indications. For example, Moexipril, an ACE inhibitor [34], showed a proper binding mode via hydrophobic interactions and a hydrogen bond through a carboxylic acid moiety with Gln189 at S score – 13.2142 Kcal/mol. Daunorubicin and Mitoxantrone are representatives for anthracene glycosidic chemotherapeutic agents [35,36]. Daunorubicin showed potential binding affinity via hydrophobic interactions and hydrogen bonding with Asn142 and Glu166. Mitoxantrone showed hydrophobic interactions and a network of hydrogen bonds with His41, His164, Asp187, Thr190, and Gln192. The anthracene derivatives findings suggest that glycoside-based derivatives can target the substrate-binding pocket of SARS-CoV-2 Mpro. However, administration of chemotherapeutic agents can lead to significant adverse effects and is unlikely to be of any clinical utility in critically ill COVID-19 patients. Metamizole, a pyrazolone based derivative [37], showed a potential binding affinity via hydrogen bonds between a sulphonic acid moiety and His 163 and Ser144 in addition to pi-pi interaction with His41. Although metamizole might have clinical utility, it is also not an ideal candidate due to its association with agranulocytosis, which would be an unwelcomed side effect in COVID-19 patients. Bepotastine, an anti-histaminic [38,39], exhibited proper binding affinity in the main substrate-binding pocket via hydrophobic interactions and hydrogen bonding through a carboxylic acid moiety with Gln189. Atovaquone, an anti-malarial drug [40], showed a potential binding affinity with no hydrogen bonds with an S score – 8.4159 Kcal/mol. Rosuvastatin, which belongs to the statins class of antihyperlipidemic drugs [41] displayed an excellent binding affinity in terms of free energy with an S score of – 12.3096 Kcal/mol. The Rosuvastatin skeleton filled the entire substrate-binding pocket via hydrophobic interactions and hydrogen bonding with Gly143 and Glu166. Thus, structure-based drugs design for identifying the top hits targeting the central site of the substrate binding pocket elucidated the following preliminary pharmacophore features: (1) The entire pocket needs hydrophobic features or extended phenyl moieties to maintain a proper binding affinity such as in case of anthracene derivatives. (2) A network of hydrogen bonds (whether donors or acceptors) is a significant factor especially with amino acids Glu166, Gln189, His163, and His164. (3) The presence of terminal sulphonic acid and/or carboxylic acid moieties (Bepotastine, Moexipril, Metamizole, and Rosuvastatin) can act as bio-isosteric moieties to the phosphate groups that can be found in antiviral drugs.

Terminal site molecular docking: The results of docking at the terminal site of the Mpro substrate-binding pocket revealed 8 top hits based

Table 1

List of top drugs docked to the central domain of COVID-19 virus M^{pro} substrate-binding pocket based on S score.

Drug	S score (Kcal / mol)	Clinical Indication
Darunavir	-14.0304	Antiviral
Mitoxantrone	-13.8100	Anticancer
Nelfinavir	-13.4200	Antiviral
Moexipril	-13.2442	Anti-hypertensive
Daunorubicin	-12.5009	Anticancer
Rosuvastatin	-12.3096	Anti-hypercholesterolemia
Saquinavir	-12.0917	Antiviral
Metamizole	-11.6652	Anti-inflammatory
Bepotastine	-10.6350	Anti-histaminic
Benzonate	-10.4759	Anti-tussive
Atovaquone	-8.1459	Antimalarial

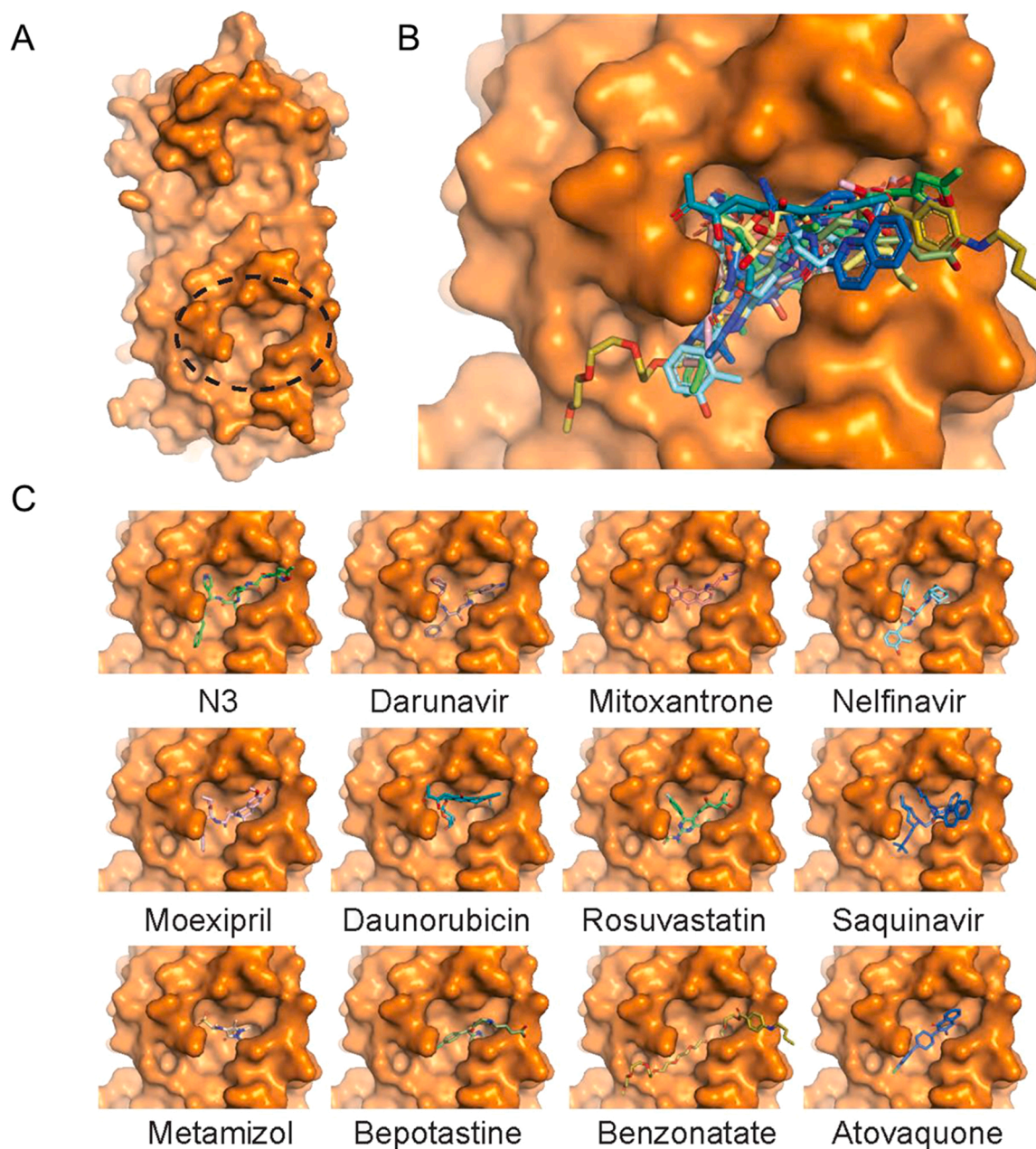


Fig. 1. Docked positions to the central site of the substrate binding-pocket of SARS-CoV-2 Mpro: (A) 3D presentation of the pocket. (B) Overlaid docked positions of all 11 top hits in addition to the previously co-crystallized inhibitory peptide N3. (C) Individual docking positions.

on their S score, binding affinity, interacting amino acids, and binding mode to fit the terminal portion and with respect to the reported clinical indication, as shown in [Table S2](#). Our three and two-dimensional analyses for the top hits targeting the terminal site are shown in [Figs. S2 and S3](#). Montelukast, an anti-asthmatic drug, showed the best binding affinity in terms of hydrophobic-hydrophobic and hydrogen bond interactions with Thr24, Ser46, and Gln189 at S score -11.8226 Kcal/mol. A recent report also showed the binding affinity of Montelukast to the same binding domain [42]. Lisinopril, an ACE inhibitor, showed proper binding mode via hydrophobic interactions and a hydrogen bond through a carboxylic acid and amine moieties with Thr26 and His164, respectively at S score -11.5878 Kcal/mol. Bumetanide, a loop diuretic showed a hydrogen bond network with Ser144, His163, Glu166, and Gln189; in addition to pi-pi interaction along with His41 at S score -11.3008 Kcal/mol. Fexofenadine, an anti-histaminic, protrudes towards the terminal groove of the protease binding pocket with

hydrophobic-hydrophobic interactions and hydrogen bond with Thr26 at S score -10.8085 Kcal/mol. Pirbuterol, another anti-asthma with β_2 adrenergic activity, bound to the terminal site without further protrusion towards the center with hydrogen bonds Thr24, Thr25, and Ser46. Finally, Bosentan, an endothelin receptor antagonist used for pulmonary arterial hypertension, and quinidine showed hydrophobic interactions with no hydrogen bonds at S score -10.0878 Kcal/mol and -9.0607 Kcal/mol. Although the dimensional size of the terminal site is limited compared to the central site for the Mpro substrate-binding domain, the key amino acid residues for binding are Thr24, Thr25, Thr26, and Ser46.

Covalent molecular docking: Finally, we performed an independent covalent docking study to identify FDA drugs that can target the catalytic amino acid Cys145 within the substrate-binding pocket, especially given that the co-crystallized inhibitor is peptide in nature (α ketoamide) with covalent mode of binding [43]. We screened the top 200 drugs that resulted from the central and terminal molecular docking (top

100 for each) for targeted covalent docking through Cys145 via DOCKTITE's protocol by Molecular Operating Environment (MOE) [44]. This resulted in identifying 30 drugs that demonstrated possible nucleophilic attack by Cys145 and undergo covalent docking to generate R and S stereoisomers (Table 2). Only 9 candidates showed promising binding affinity with respect to S score and covalent binding ability. Our three and two-dimensional analysis for the top 9 covalent hits targeting Cys 145 is shown in Fig. 2 and Figs. S5 and S6.

Antiviral activity assay: After completing *in silico* docking studies, we next used a cell-based assay to test the antiviral activity of selected compounds against SARS-CoV-2. An isolate of SARS-CoV-2 (USA-WA1/2020) was obtained and propagated in Vero E6 cells [45]. For initial drug screening, Vero E6 were infected with SARS-CoV-2 at 0.1–0.25 multiplicity of infection (MOI). After 1 hr, media containing drugs covering a 6-log₁₀ dilution series was added to the cells. Total RNA from virally infected cells was isolated 24 h post-infection and viral RNA replication was quantified by RT-qPCR using TaqMan probes. In parallel studies, drugs were screened for effects on cell viability and cellular metabolism by quantifying lactate dehydrogenase (LDH) release and cellular ATP levels (Cell Titer Glo), respectively.

From the 11 drugs identified by the central site docking method, we observed dose-dependent inhibition of SARS-CoV-2 with Atovaquone, Mitoxantrone, Daunorubicin, and Nelfinivir (Fig. 3). LDH release assays showed that Daunorubicin and Nelfinivir were toxic to cells at high doses, whereas Atovaquone and Mitoxantrone did not elicit substantial LDH release. Of the 7 of the drugs identified by the terminal site docking method, Quinidine, and Bosentan exhibited modest dose-dependent antiviral effects with minimal impact on LDH release and cellular ATP levels (Fig. S6). Quinidine was reported in another drug screening study as a candidate antiviral for SARS-CoV-2 [46]. Of the top 7 of drugs that were predicted to exhibit covalent binding, we observed dose-dependent inhibition with Atovaquone, Ouabain, Dronedarone, Mebendazole, and Dronedarone, although Dronedarone appeared to be particularly toxic at IC₅₀ concentrations (Fig. 4a). Interestingly, Ouabain and digoxin, which are cardiac glycosides, have recently been reported to inhibit SARS-CoV-2 infection [47,48]. Together, 3 of the 7 covalent docking drugs (Atovaquone, Ouabain, and Mebendazole) exhibit antiviral effects in the absence of overt toxicity, suggesting a reasonable hit rate for the *in-silico* analysis (Fig. 4b).

We next sought to validate several covalent docking candidates and determine cytotoxicity concentration at 50% (CC₅₀s) and inhibitory viral replication concentration at 50% (IC₅₀s) over a 10 pt-dose response (Table 3). Viral infections were performed as described above in Vero E6 and human hepatoma Huh7.5 cells, followed by treating cells with 3-fold dilutions of Atovaquone, Ouabain, Dronedarone, and Mebendazole, starting at 100 μM, or in one set of experiments, 200 μM Atovaquone. In both cell lines, all drugs tested showed CC₅₀ > 100 μM, except dronedarone showed CC₅₀ against Vero E6 and Huh7.5 at 22.70 and 20.20 μM, respectively. In addition, the tested drugs recapitulated initial findings, though Mebendazole had less antiviral activity in

Table 2

List of top drugs docked covalently to Cys 145 of COVID-19 virus Mpro substrate-binding pocket showing the configuration of nucleophilic attack and S score.

Drug	Stereogenic center orientation	S score (Kcal / mol)	Clinical Indication
Dronedarone	R	-12.8752	Antiarrhythmic
Mitoxantrone	R	-11.6140	Anticancer
Tipranavir	S	-11.3686	Antiviral
Idarubicin	R	-10.1043	Anticancer
Atovaquone	R	-8.8177	Antimalarial
Ouabain	S	-8.4562	Anticancer
Entacapone	R	-8.2882	COMT inhibitor
Metamizole	R	-82165	Anti-inflammatory
Mebendazole	R	-7.5352	Anti-parasite

Huh7.5 cells as compared to Vero E6 cells. We determined the following IC₅₀s: Atovaquone (1.5 μM in Vero E6, 6.8 μM in Huh7.5); Ouabain (0.030 μM in Vero E6, 0.075 μM in Huh7.5); Dronedarone (1.5 μM in Vero E6, 0.38 μM in Huh7.5); Mebendazole (0.25–1.2 μM in Vero E6, but lacks strong inhibitory activity on Huh7.5 cells). In addition, we sought to visually demonstrate the antiviral effect of Atovaquone by indirect immunofluorescence, staining for virus-generated double-stranded RNA (dsRNA), a replication intermediate during coronavirus genome amplification, using a dsRNA-specific monoclonal antibody. We tested Atovaquone at 2.5 μM and 7.5 μM in Vero E6 cells and at 10 μM in Huh7.5 cells transduced with lentivirus expressing the SARS-CoV-2 receptor ACE2. Drug-treated cells showed a striking reduction in dsRNA staining as compared to DMSO-treated control cells (Fig. 4c). Data from DrugBank suggest that atovaquone is very highly protein bound (>99.9%) [49]. To facilitate comparison of cell culture data with achievable therapeutic concentrations of atovaquone, we measured protein binding for this compound in tissue culture media and mouse and human plasma. Using rapid equilibrium dialysis, the unbound fraction (fu) of atovaquone was 0.0008 in tissue culture media containing 10% FBS, 0.00003 in human plasma, and 0.0001 in murine plasma (Table S5). This suggests the free IC₅₀ may be as low as 1.2 nM for Vero E6 cells. To validate this measurement, we repeated the antiviral assay in WHO Vero, a cell line adapted for serum-free growth. Under these conditions, the IC₅₀ was 20 nM (Fig. 4d). As nonspecific binding to plasma proteins is a reversible event [50], it is not surprising that more drug may be locally available to bind a target that likely has a higher affinity, suggesting a possible reason for the discrepancy in values. However, for the purposes of comparing free drug levels *in vitro* and *in vivo*, we have used values based on the fu.

Mpro protein purification and activity assays:

Next, we purified M^{pro} protein to determine the potential of the above-mentioned candidates to inhibit its activity, as previously described [51]. Initially, we screened 9 drugs for their Mpro inhibitory profiles by pre-incubating them at a single concentration (50 μM) in the presence of 0.2 μM Mpro and 0.1 mM DTT for 90 mins, followed by adding Mpro fluorogenic substrate, using wavelengths of 360 nm and 460 nm for excitation and emission, respectively. Only entacapone and dronedarone showed 50% inhibition for the Mpro activity under these conditions. Next, we tested the effect of longer residence time on Mpro activity by incubating the candidate drugs for 12 h with the purified protein, which demonstrated that entacapone, dronedarone, and mebendazole showed significant inhibition for the Mpro activity. However, atovaquone (50 μM) demonstrated only a modest inhibitory effect of ~35% on Mpro activity (Fig. 5a). We subsequently screened entacapone, dronedarone, mebendazole at 10-dose levels against Mpro activity which demonstrated IC₅₀ values of 9.04 μM, 18.03 μM, and 19.94 μM, respectively (Fig. 5b). Finally, we used tandem mass spectrometry analysis to identify potential covalent inhibitors targeting Mpro. We found that only entacapone demonstrated evidence of covalent modification of Mpro, where 15–20% for Mpro was covalently modified (Fig. 5c). Collectively these results indicate that several of our top molecular docking hits exhibited Mpro inhibitory activity, but only entacapone showed evidence of covalent modification of Mpro.

Atovaquone does not inhibit pyrimidine de-novo synthesis in Vero E6 cell lines at 1 μM and 5 μM:

Atovaquone is an attractive repurposing candidate given its safety and pharmacokinetic profile. However, since our assays failed to demonstrate a meaningful inhibitory effect of atovaquone against the purified Mpro protein at concentrations relevant to its antiviral IC₅₀, we sought to determine other potential antiviral mechanisms of atovaquone. Atovaquone is known to inhibit dihydroorotate dehydrogenase (DHODH), an enzyme required for *de novo* pyrimidine synthesis, leading to specific depletion of intracellular nucleotides and eventually resulting in inhibition of viral replication of arthropod-borne viruses (such as ZIKV and chikungunya virus) [52–54]. Therefore, we examined whether the antiviral effect of atovaquone is mediated by inhibition of DHODH.

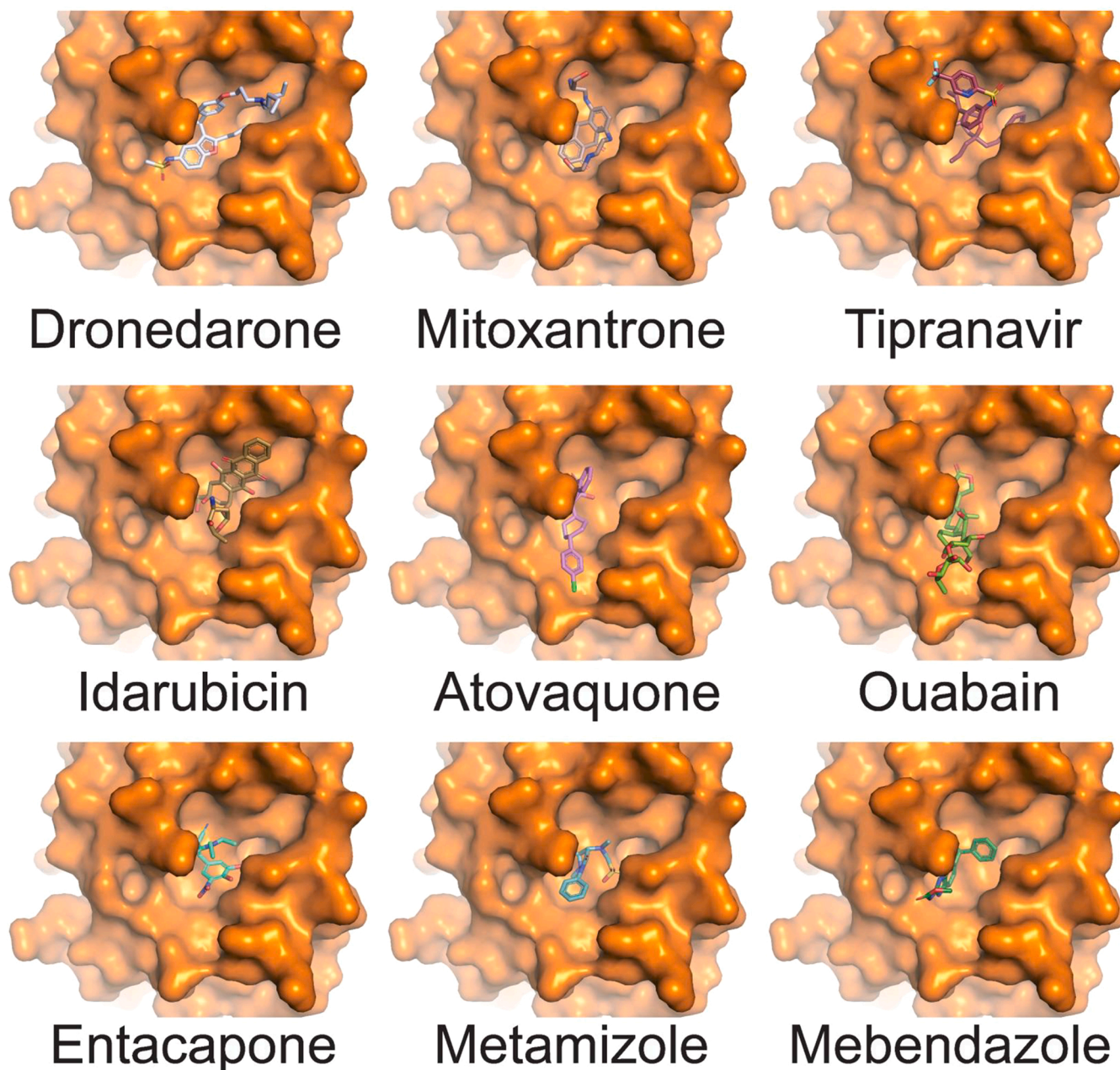


Fig. 2. Docked positions for the covalently bound candidates targeting Cys145 of SARS-CoV-2 Mpro.

First, we performed metabolomic analysis of atovaquone-treated host (Vero E6) cells at 1 μM and 5 μM . The metabolomic profile demonstrated that atovaquone does not inhibit pyrimidine synthesis at concentrations relevant to the observed antiviral IC50s, as there was no significant change in the uridine 5'-mono-phosphate (UMP) levels versus orotate and dihydroorotate levels, compared to DMSO-treated cells. Consistent with published reports, we observed significant inhibition in pyrimidine synthesis at 10 μM (~10-fold higher the IC50) (Fig. 6). Second, we examined viral replication in the presence of 5 μM and 100 μM uridine treated with 1.5, 5, and 10 μM atovaquone or 5 μM vidofludimus (a selective DHODH inhibitor). In this scenario, uridine should reverse the observed inhibitory effect on viral replication if it is mediated by inhibition of pyrimidine synthesis. We found that atovaquone showed significant inhibition for viral replication regardless the uridine concentration, however vidofludimus inhibitory activity was reversed with addition of uridine. Collectively, these results demonstrate that the observed antiviral effect of atovaquone is likely not

mediated by inhibition of DHODH.

2.1. Atovaquone inhibits purine de-novo synthesis in vero-E6 cell lines at 1 μM and 5 μM

The metabolomic profile also demonstrated that atovaquone-treated cells showed significant depletion in the free guanosine, inosine, and adenosine; at both 1 and 5 μM , suggesting that atovaquone targets host purine biosynthesis cell at concentrations equivalent to its antiviral IC50s. Therefore, we examined the protein expression levels of ecto-5'-nucleotidase (NT5E) or (CD73), which is a key enzyme that catalyzes the conversion of GMP, IMP an AMP to guanosine, inosine and adenosine respectively. Interestingly, we found that NT5E expression was significantly downregulated in atovaquone treated cells. These results indicate that atovaquone inhibits purine synthesis through downregulation of NT5E, which may represent a novel mechanism of action of atovaquone that can be relevant to a wide range of indications (Fig. 7).

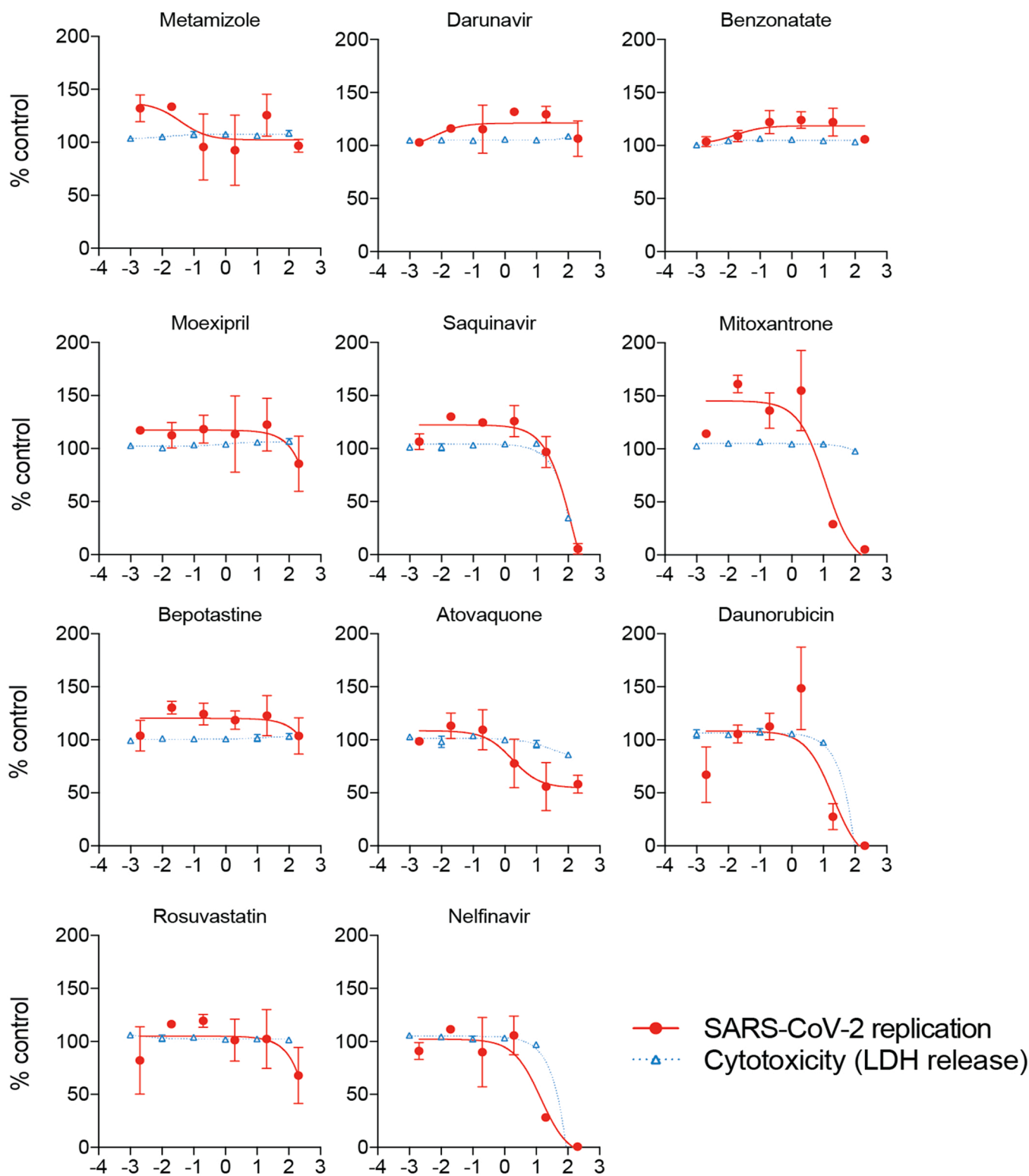


Fig. 3. Antiviral activity of drugs identified by central site docking for Vero E6 cells infected with SARS-CoV-2. SARS-CoV-2 replication was quantified by TaqMan RT-PCR. Drug-induced effects on cells was monitored by quantifying LDH release and ATP levels. Data represent the averages of two biological replicates. Error bars, SEM.

Atovaquone and Mebendazole does not induce phospholipidosis in Vero E6 cells at 1 μ M and 5 μ M: Recently, an elegant study reported that phospholipidosis induced by cationic amphiphilic drugs can inhibit SARS-Cov-2 viral replication in cells [55]. Hence, we investigated the potential association between the anti-viral activities exhibited by atovaquone and mebendazole and induction of phospholipidosis. Our

interest to address the cellular mechanism for mebendazole was motivating to look at potential of -NH of benzimidazole ring to form cationic amphiphilic species in physiological environment. Therefore, we tested the phospholipidosis effect by treating Vero E6 cells with atovaquone and mebendazole at 1, 5, and 10 μ M using the well-established nitro-benzoxadiazole-conjugated phosphoethanolamine (NBD-PE) staining

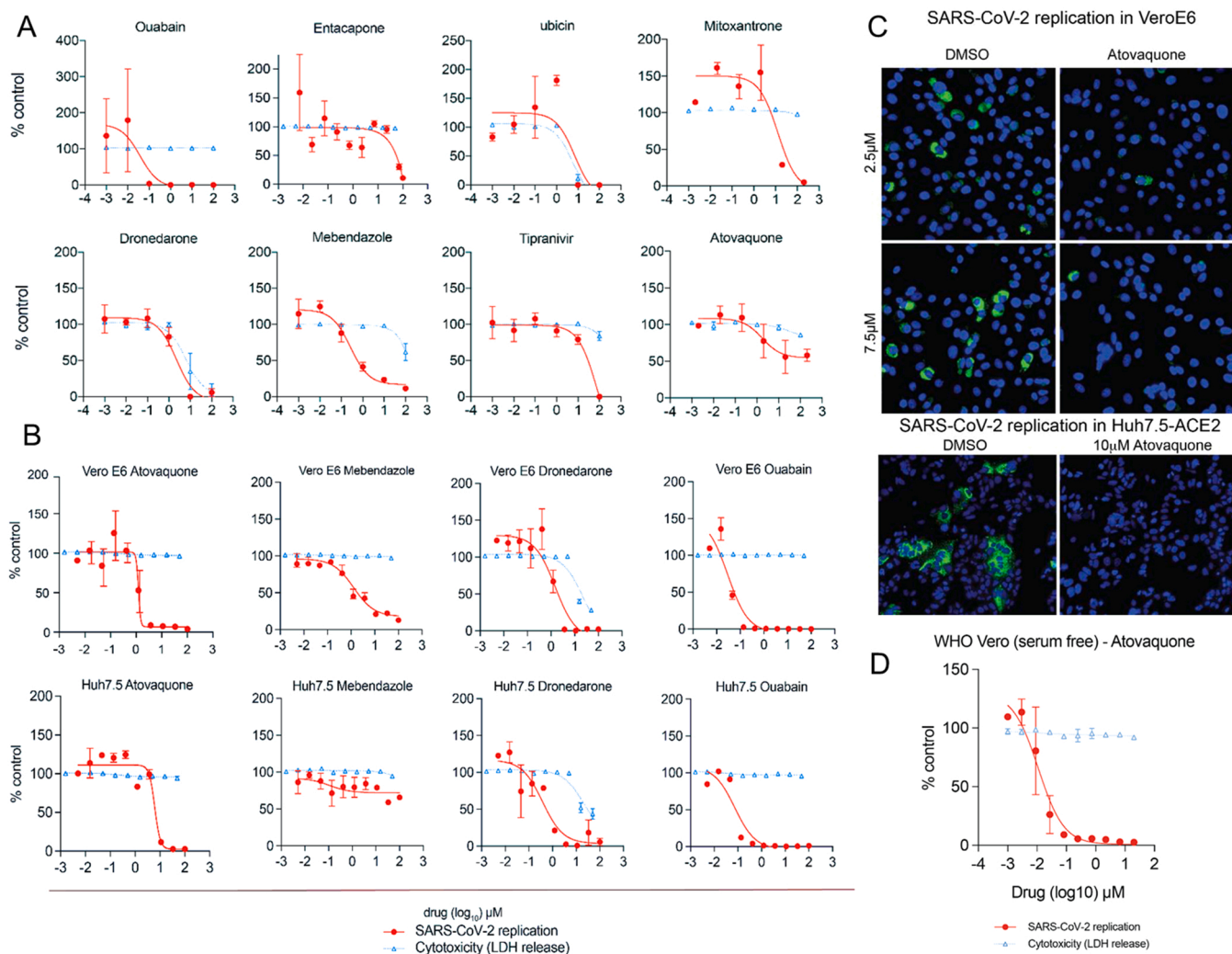


Fig. 4. (A) Antiviral activity of drugs predicted to covalently bind to Mpro active site for Vero E6 infected with SARS-CoV-2. SARS-CoV-2 replication was quantified by TaqMan RT-PCR. Drug-induced effects on cells was monitored by quantifying LDH release and ATP levels. Data represent the averages of two biological replicates. Error bars, SEM. (B) Validation of antiviral activity of atovaquone, mebendazole, dronedarone, and ouabain by 10 pt curve analysis in Vero E6 and Huh7.5 cells infected with SARS-CoV-2. SARS-CoV-2 replication was quantified by TaqMan RT-PCR. LDH data are duplicated from previous figures. DMSO is shown as a control for effects of vehicle on infection in Huh7.5 cells. Data represent the averages of three biological replicates for Atovaquone "second viral prep" and two replicates for all others. Error bars, SEM. (C) Cells were stained with anti-dsRNA antibody 24 h post-infection. N = 1. B. Huh7.5 cells ectopically expressing ACE2 were treated with one dose of Atovaquone 1 h after infection with SARS-CoV-2. Cells were stained with anti-dsRNA antibody 10 h post-infection. Data are representative of images obtained from 1 (Vero E6) or 2 (Huh7.5) independent experiments. (D) Antiviral activity of atovaquone in Vero E6 cells infected with SARS-CoV-2 under serum-free conditions.

Table 3

CC50 and IC50 profile for selected drugs against Vero E6 and Huh7.5 cells infected with Sars-CoV-2.

Drug	Vero E6		Huh7.5	
	EC50(μM) (R ²)	CC50(μM) (R ²)	EC50(μM) (R ²)	CC50(μM) (R ²)
Atovaquone	1.20 (0.84)	> 100	6.20 (0.93)	> 100
Mebendazole	1.30 (0.95)	> 100	ND	> 100
Dronedarone	1.50 (0.86)	22.70 (0.91)	0.38 (0.83)	20.20 (0.90)
Ouabain	0.03 (0.89)	> 100	0.07 (0.90)	> 100
Digoxin	0.07 (0.91)	> 100	NA	NA
Entacapone	ND	> 100	NA	NA

ND: Not determinable from available data.

NA: Not assayed.

assay [56]. Mebendazole-treated Vero E6 cells did not induce phospholipidosis at 1 and 5 μM, however there was a significant increase in the NBD-PE quantification of phospholipidosis at 10 μM (Fig. 8). This

suggested that the anti-viral activity shown by mebendazole is not due to phospholipidosis. Meanwhile, atovaquone-treated Vero E6 cells did not show phospholipidosis at 1–10 μM, this was coming in agreement with our expectations due to the lack of quaternary ammonium center in the atovaquone chemical structure.

2.2. Atovaquone can distribute to lungs and epithelial lining fluid (ELF)

Next, we performed a series of pharmacokinetic (PK) studies to determine atovaquone levels in the plasma and epithelial lining fluid (ELF) to determine whether therapeutic atovaquone levels can be achieved clinically. Mice were treated with 20 mg/kg PO daily for 7 days, which was followed by measuring total plasma atovaquone, free plasma atovaquone, and free ELF atovaquone concentrations. We chose this schedule because a preliminary analysis suggested a half-life for atovaquone in mice of approximately 18–38 h, so we sought to achieve steady state for our analyses. With this dose and schedule, total plasma concentrations peaked at 100 μg/mL and free plasma levels peaked at

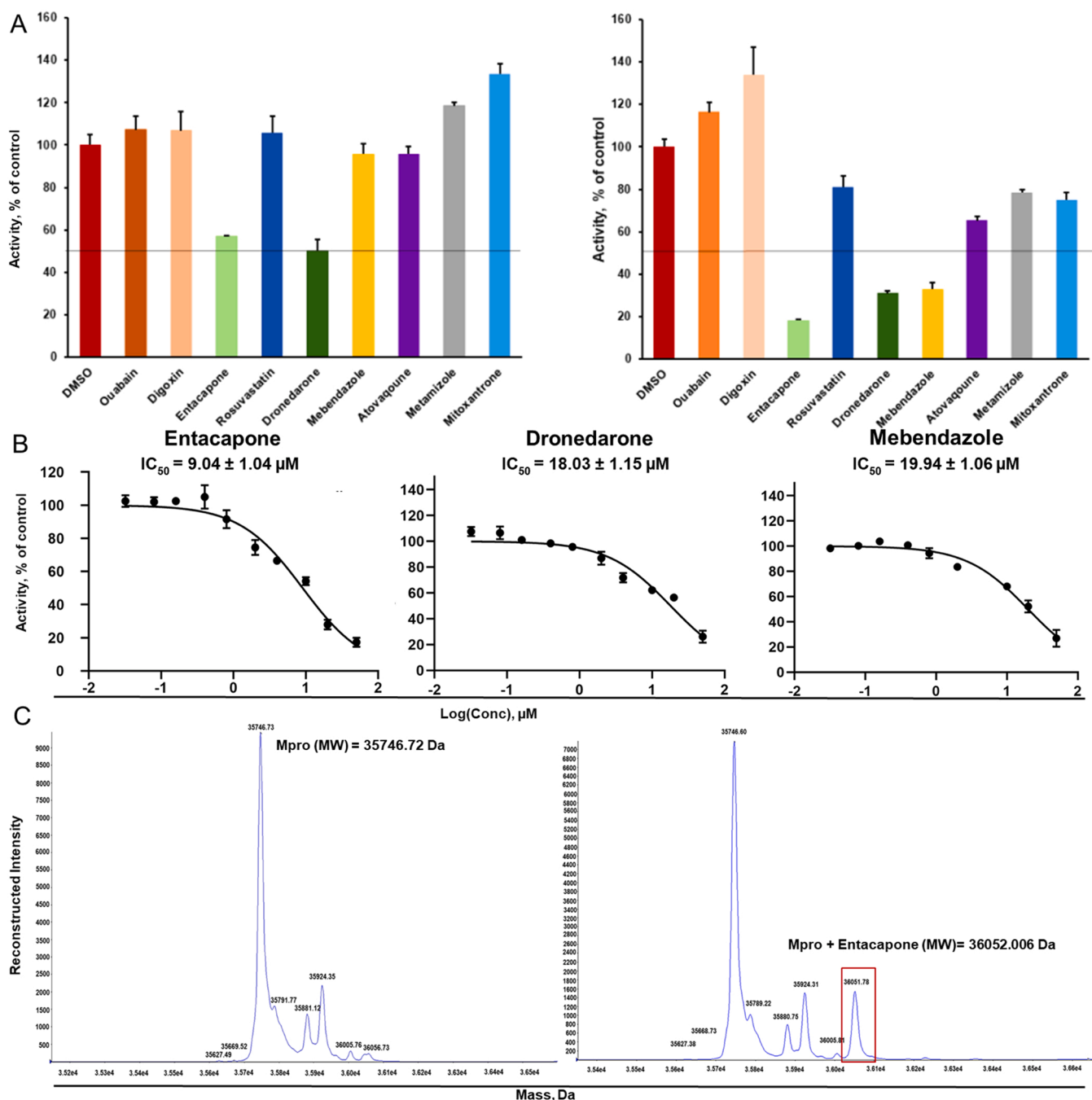


Fig. 5. (A) Effect of residence time of pre-incubation of 0.2 μM Mpro in the presence of 1 mM DTT and the selected drugs at concentration of 50 μM (90 mins and 12 h) on Mpro activity, DMSO concentration did not exceed 10%. This was followed by adding fluorogenic substrate to measure fluorescence intensity using microplate reader at wavelengths of 360 nm and 460 nm for excitation and emission, respectively. Data represent average of triplicates. Error bars, SEM. (B) Dose-response curve for entacapone, dronedarone, and mebendazole to elucidate IC₅₀ using GraphPad Prism. Data represent average of duplicates. Error bars, SEM. (C) Intact mass analyses for Mpro and Mpro incubated with entacapone at a ratio of (1:100), followed by tandem mass spectrometry.

approximately 16 ng/mL (44 nM). Free epithelial lining fluid (ELF) concentrations were similar to free plasma levels, peaking at 25 ng/mL (70 nM) (Fig. 9A). We followed the standard practice of normalizing drug concentrations found in bronchial lavage fluid (BAL) by urea concentrations in plasma and BAL in order to determine ELF concentrations.

To translate these observations to human, we found that the maximum plasma concentration (C_{max}) was higher compared to the reported single dose of atovaquone human oral suspension and approximately 2–5-fold higher compared to BID dosing in HIV infected volunteers [57]. Assuming linear PK in mice and similar biodistribution

in human ELF, total human plasma concentrations of 15 $\mu\text{g/mL}$ (41 μM), may yield free plasma and ELF drug levels of at least 1.2 nM, close to the free IC₅₀ for SARS-COV-2 determined based on free drug in tissue culture media. This plasma level is within observed steady state concentrations for atovaquone in HIV positive individuals [58,59].

2.3. Mebendazole achieves IC₅₀-relevant concentrations in ELF

We also performed PK studies to determine mebendazole levels in plasma, lungs, and ELF. Although we did not anticipate the same long half-life for mebendazole, we followed the same dosing schedule as

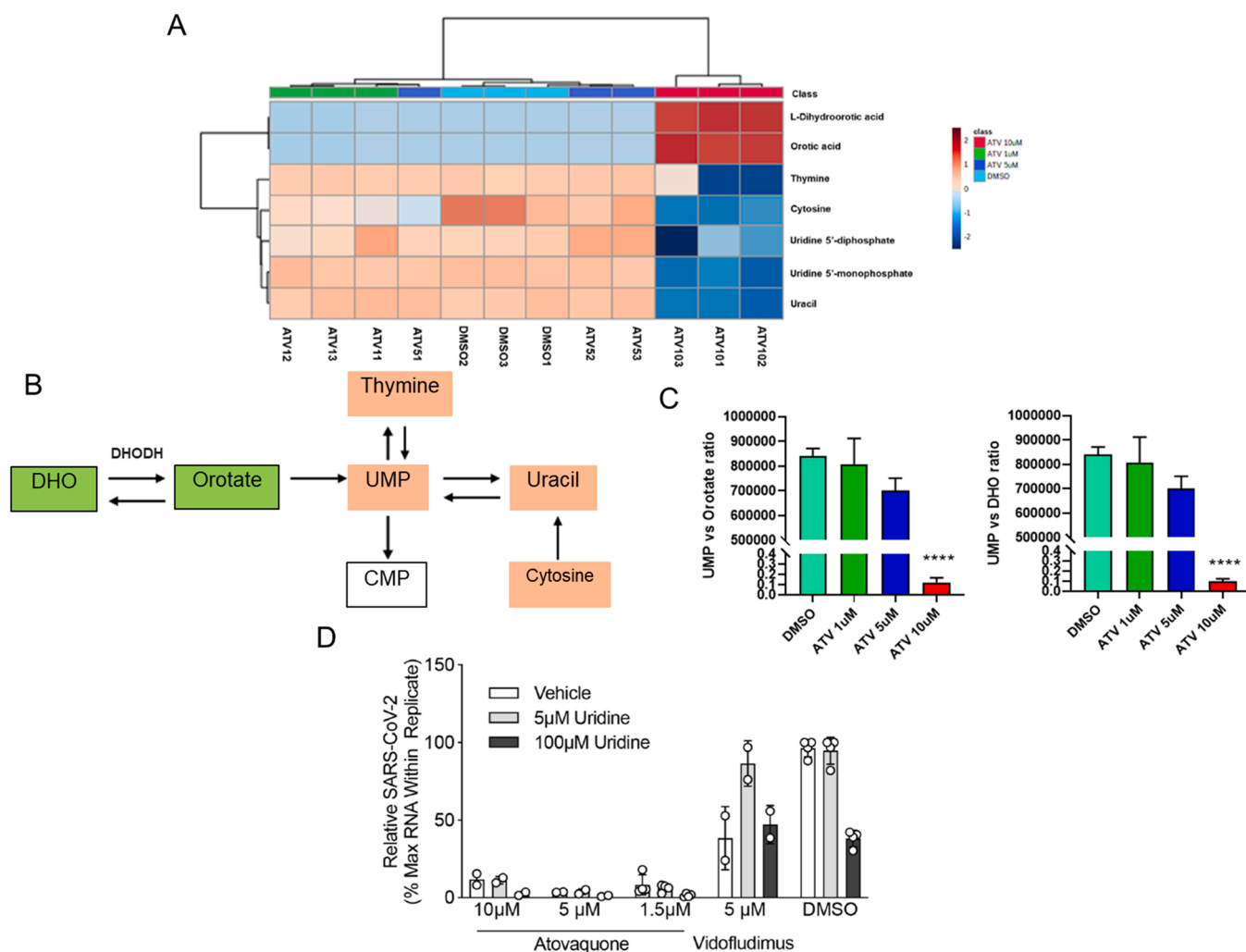


Fig. 6. Atovaquone does not target pyrimidine synthesis pathway Vero E6 cells at 1 and 5 μM. (A) Metabolomic analyses for Vero E6 cells treated with DMSO or Atovaquone, at, showing no change in the uridine monophosphate (UMP) levels at 1 and 5 μM, and significant depletion in UMP levels at 10 μM. (B) Molecular pathway of de novo pyrimidine synthesis. (C) Levels of UMP with respect to orotate and dihydroorotate levels in Vero E6 cells treated with 1, 5, and 10 μM atovaquone, showing only depletion in the UMP levels at 10 μM ATO. (D) SARS-CoV-2 replication in the presence of 5 μM and 100 μM uridine treated with 1.5, 5, and 10 μM atovaquone or 5 μM vidofludimus (potent DHODH inhibitor). Atovaquone showed significant inhibition for viral replication regardless of the uridine concentration, however vidofludimus activity changed based on the uridine addition. Data represent average of biological triplicates. Error bars, SEM.

atovaquone for consistency, treating mice with 10 mg/kg PO daily for 7 days. Subsequently, total plasma, free plasma, and free ELF levels of mebendazole were measured. We found that the maximum total plasma concentration was high within 90 mins after the last dose, with an average of 697.67 ng/mL (equivalent to 2.36 μM). Based on our determined free fraction of mebendazole in mouse plasma (Table S5), this gives rise to a maximum free drug concentration of approximately 90 ng/mL (305 nM). Interestingly, free drug levels in ELF were higher, nearing 550 ng/mL (1.8 μM) at peak, suggesting that it is within the observed free antiviral IC₅₀ of Vero E6 cells (Fig. 9B). Plasma exposures noted here in mice are generally higher than those noted in the literature for humans receiving mebendazole. Peak plasma levels of patients receiving 10 mg/kg every 6 h (total 40 mg/kg/day) reach only 0.3–1.69 μM [60]. Higher doses have been shown to demonstrate improved exposure [61], so it is possible therapeutic concentrations may be achieved.

3. Discussion

In the current report, we were the first in March 2020, to demonstrate that screening FDA approved drugs against the SARS-CoV-2 virus

Mpro substrate-binding pocket can identify candidate drugs with antiviral activity against SARS-CoV-2 in cultured cells. This approach provides a valuable road map to fast-track drugs with established safety profiles to clinical trials. We have concluded our prospective randomized placebo controlled clinical trial for testing the use of atovaquone in patients hospitalized with COVID-19 [62]. Our clinical trial showed that atovaquone did not meet the primary endpoint of a significant effect on SARS-CoV-2 viral clearance compared with placebo. However, based on the observed inverse correlation between atovaquone levels and viral load, additional PK-guided studies showed that the antiviral effect of atovaquone is dependent on the body-mass index in COVID-19 patients. Nevertheless, there are several limitations of the current study that are worth discussing.

Only 3 of our top 30 hits, dronedarone, mebendazole, and entacapone, demonstrated measurable inhibitory activity against Mpro using purified protein in an enzymatic assay. In addition, only entacapone showed evidence of covalent modification of Mpro by mass spectrometry, although it did not elicit a reproducible antiviral effect in cultured cells and thus an IC₅₀ for this drug could not be calculated. Dronedarone is unlikely to have a real therapeutic value given that its antiviral activity tracks with its cellular toxicity, and its therapeutic

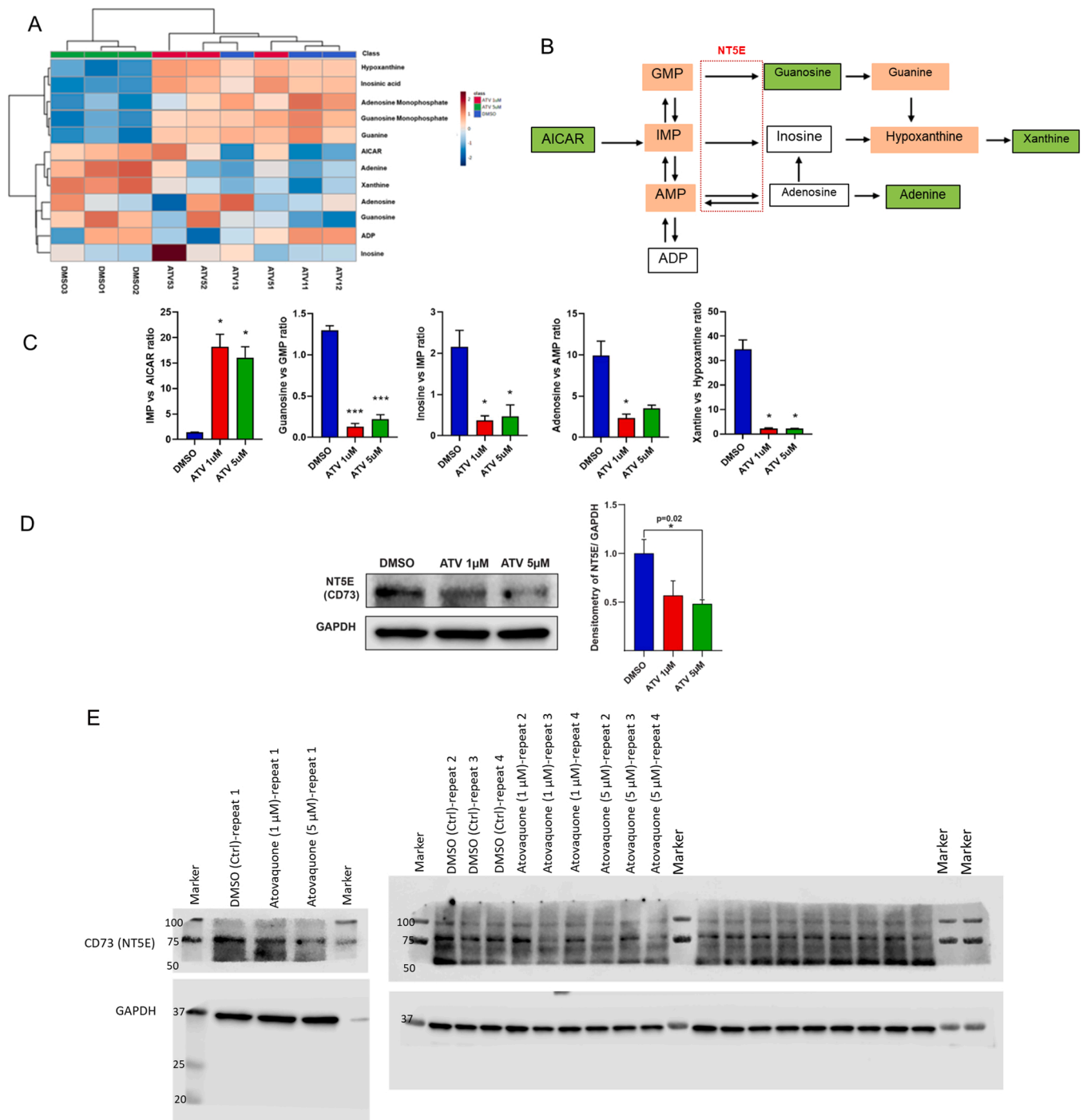


Fig. 7. Atovaquone targets purine synthesis pathway for the Vero E6 cells at 1 and 5 µM. (A) Metabolomic analyses for DMSO and Atovaquone treated Vero E6 cells at 1, 5, and 10 µM, showing downregulation of adenosine, guanosine, and inosine levels. (B) Molecular pathway of de novo purine synthesis. (C) Levels of free guanosine, inosine, and adenosine with respect to GMP, IMP, and AMP at Vero-E6 cells treated with 1 and 5 µM ATO. (D) Left Panel: Representative WB of NT5E in vehicle and Atovaquone treated cells. Right Panel: Quantification of NT5E protein expression demonstrating a significant decrease in cells treated with 5 µM Atovaquone. (E) WB of CD73 (NT5E) in vehicle and Atovaquone treated cells for independent replicates.

plasma concentration (less than 300 nM [63]) is significantly lower than the measured IC₅₀ of 1.5 µM. Mebendazole showed moderate inhibitory profile against Mpro and potent antiviral activity with IC₅₀ of 0.25–1.2 µM in Vero E6 cells although it appears less effective in the human cell line Huh7.5 and thus further studies on other types of human cells are needed. It is unclear if therapeutically active concentrations against SARS-CoV-2 can be achieved in patients with a sufficiently high

dose. Interestingly, ouabain had an IC₅₀ against SARS-CoV-2 in the low nanomolar range, which is well within its therapeutic concentration [64]. However, ouabain, along with digoxin, both Na⁺/K⁺ ATPase inhibitors, have a very narrow therapeutic index, which may limit their use in critically ill patients, especially those with impaired renal function or significant electrolyte abnormalities.

As outlined earlier, atovaquone and mebendazole are the leading

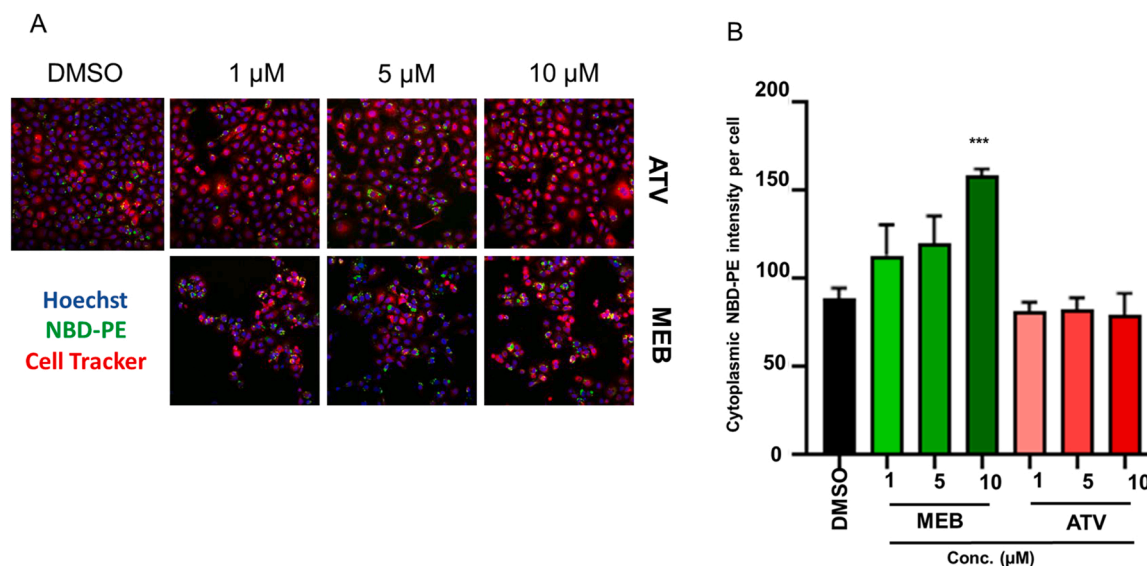


Fig. 8. Cellular Phospholipidosis assay for Vero E6 cells treated with atovaquone and mebendazole. (A) Examples of NBD-PE quantification of Phospholipidosis in Vero E6 cells treated with DMSO, atovaquone, and mebendazole (1–10 μM). Blue indicates Hoechst nuclei staining, red indicates cellTracker, and green indicates NBD-PE phospholipid staining. (B) Quantification of NPD-PE intensity per cell for DMSO, atovaquone, and mebendazole treated Vero E6 cells, showing significant induction of phospholipidosis at Vero E6 cells treated with 10 μM mebendazole, compared to DMSO, * ** $P = 0.0001$. Data represent average of biological triplicates. Error bars, SEM.

candidates for repurposing based on their IC₅₀, established safety profile, and PK properties. We performed additional PK studies to determine whether levels of these two drugs in airway epithelium reaches SARS-CoV-2 IC₅₀ concentrations. We found that both drugs may achieve sufficient concentrations to be therapeutically meaningful, however it is worth noting here that our BAL urea concentrations were atypically low compared to previously published studies [65], potentially due to the use of CO₂ for euthanasia which may affect lung permeability [66]. As urea normalization is used to convert the concentration of drug in BAL to a concentration in epithelial lining fluid (ELF), this could erroneously result in over estimation of ELF levels of both drugs. To evaluate this, we compared urea levels in the BAL of mice euthanized with CO₂ (5.4 + 3.7 μg/mL, n = 3) versus exsanguination under isoflurane anesthesia (3.4 + 0.7 μg/mL, n = 3) and did not note significant differences here or in plasma (data not shown). However, there may be other factors that have influenced urea values, which may affect calculated drug concentrations in ELF. In addition, although serum levels of atovaquone can reach an excess of 40 μM, and has a high volume of distribution which results in its tissue accumulation [67,6869], atovaquone is highly bound to plasma proteins. Therefore, it was important to determine both its IC₅₀ against SARS-CoV-2 in serum free conditions, as well as to determine its free levels in vivo. Our results indicate that atovaquone inhibits viral replication in serum free conditions at exceedingly low concentrations (IC₅₀ 20 nM in serum free media and calculated free IC₅₀ using fu of 1.2 nM). This free drug concentration was achievable in our PK studies in vivo in the airway epithelium, which supports a therapeutic role of atovaquone against SARS-CoV-2 that requires further clinical testing.

We also identified a potentially important new mechanism of action of atovaquone. Atovaquone does not appear to inhibit Mpro at concentrations relevant to the observed IC₅₀ against SARS-CoV-2. It is important to also note here that although atovaquone was previously shown to exert an antiviral effect on other viruses by inhibiting pyrimidine metabolism through targeting DHODH, this mechanism does not appear to be responsible for our observed antiviral effect on SARS-CoV-2. Our results however suggest that atovaquone inhibits purine metabolism, possibly through downregulation of NT5E. Although there are no current antiviral drugs known to target purine metabolism, this has been proposed to be an important target for reducing the nucleotide pool

necessary for viral replication, as well as possibly exerting anti-inflammatory effects [70]. An important limitation of the current study however is that we have not identified the mechanism by which atovaquone downregulates NT5E protein levels.

In conclusion, our screen identified atovaquone and mebendazole as our top hits for targeting SARS-CoV-2 based on their IC₅₀, PK properties, and favorable side effect profile. In addition, novel host-related mechanism targeting purine metabolism was offered. Future studies are needed to validate the mechanism of host-related purine metabolism towards targeting SARS-CoV-2 and employing further structural modifications for atovaquone skeleton to target purine metabolism for better antiviral activity against SARS-CoV-2 via different medicinal chemistry strategies.

4. Materials and methods

FDA approved small molecules preparation: The U.S. FDA approved drug database was downloaded (drugbank.ca) and 3D structures were energy minimized using MMFF94 force field.

X-ray crystal structure preparation: Crystal structure of SARS-CoV-2 Mpro co-crystallized with an inhibitor has been resolved and accessed via PDB ID: 6LU7. A box was assigned for docking procedures within the hydrophobic binding domain of the peptide inhibitor.

Structure based *in silico* screening, scoring, and validation: The whole energy minimized library was enrolled in docking simulations using Molecular Operating Environment (MOE) along with PDB ID: 6LU7 co-crystallized with N3 peptide to satisfy diverse structural iterations. The drugs were prepared by adding hydrogen addition and partial charges and energy-minimized using MMFF94 Force Field with root mean square (RMSD) gradient of 0.01 kcal/mol and RMS (Root Mean Square) distance of 0.1 Å. In addition, Mpro enzyme was prepared by removing water molecules and repeated chains. MOE QuickPrep protocol, 3D protonation, and calculation of partial charges were carried out in order to optimize structural issues. The default procedure was applied with MOE Docking protocol parameters to select the best poses with highest binding score values of the docked compounds. First, docking reliability was evaluated by extracting the co-crystallized ligand from its active site followed by re-docking into Mpro active site, and then molecular docking for selected compounds was performed, utilizing triangle

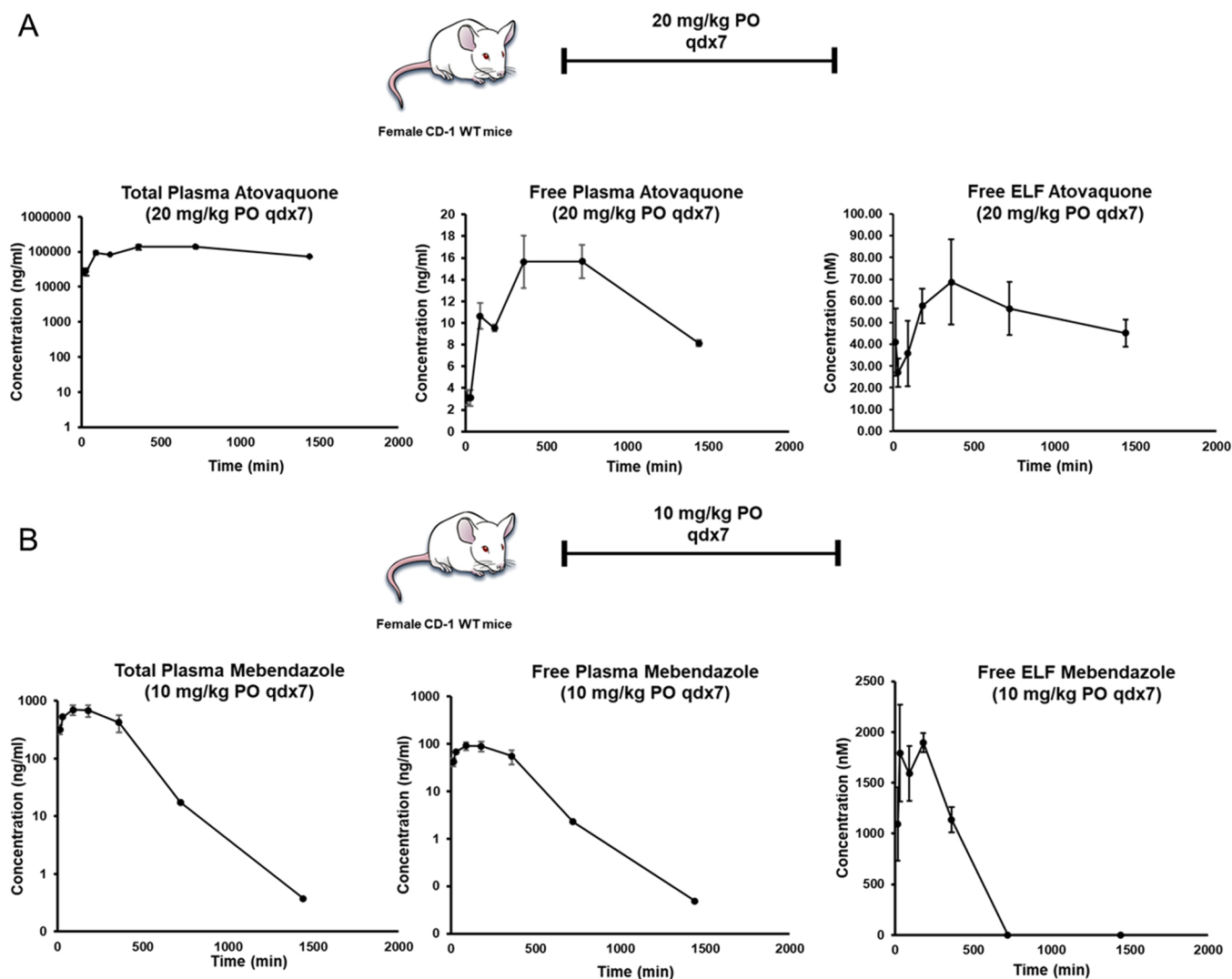


Fig. 9. Pharmacokinetics profiling for (A) Atovaquone and (B) Mebendazole.

matcher as placement method. Furthermore, the obtained docking poses were estimated and interactions with the active site were considered based on London dG scoring method to estimate energy profile based on the binding affinity with respect to hydrophobic-hydrophobic interactions [71–73]. Finally, best fitting poses into the active site expressing the best S score correlated with the best interactions with the enzyme were chosen via visual inspection. Two dimensional diagrams were generated using MOE tools, while three dimensional figures were generated using PyMOL.

Covalent Docking using DOCKTITE: We used the covalent docking protocol to filter the top 200 FDA drug candidates. The filtering step involved combining automated warhead screening to reveal 31 candidates that can undergo nucleophilic attack by Cys 145 based on their chemical structure, nucleophilic side chain attachment with the right configuration (R or S), and pharmacophore-based docking. The chimeric poses underwent consensus scoring approach using MOE-internal empirical scoring functions [74]. The validation step will include pose predictions of 10 protein/ligand complexes with a cutoff mean RMSD of 2 Å.

Virus and cells: SARS-CoV-2 (strain USA-WA1/2020) was obtained from the World Reference Center for Emerging Viruses and Arboviruses, University of Texas Medical Branch. Virus was propagated by low MOI infection (MOI 0.01–0.001) in VeroE6 cells. When 70–90% CPE was observed (48–72 h post-infection), virus-containing supernatant was

harvested, aliquot, and stored at -80°C until use. Viral titers were determined by TCID₅₀ assay. VeroE6 cells (from C. Rice, The Rockefeller University) were grown in MEM (Gibco) supplemented with 10% FBS (Gibco) and $1 \times$ non-essential amino acids (NEAA; Gibco). Huh7.5 and 293 T cells (from C. Rice, The Rockefeller University) were grown in DMEM (Gibco) supplemented with 10% FBS (Gibco) and $1 \times$ non-essential amino acids (NEAA; Gibco). Huh7.5 cells stably expressing ACE2 were maintained in DMEM supplemented with $4 \mu\text{g}/\text{mL}$ puromycin.

Lentiviral pseudo particles: Lentiviral pseudo particles were generated by transfection in 293 T cells. Lentiviral pseudo particles in the pSCRPSY backbone were generated as previously described [75]. A plasmid containing human ACE2 open reading frame was a kind gift of Neal Alto (UT Southwestern Medical Center).

SARS-CoV-2 infections: For screens, VeroE6 or Huh7.5 cells were seeded at 30,000 cells per well on 48 well plates approximately 16–20 h before infection. Prior to infection, drugs were serially diluted in media to a concentration of 1.5X target concentration. For screens, 6-point 10-fold dilutions of drug were used, and for validation 10-point 3-fold dilutions were used. Cells were incubated with 0.1–0.25 MOI SARS-CoV-2 in a minimum volume of low-serum media for one hour to allow virus to bind and enter cells. After viral entry, media containing candidate compounds or vehicle control was added to cells to a final 1X concentration. All SARS-CoV-2 infections were performed in a Biosafety Level 3

(BSL3) facility according to institutional guidelines provided by the UT Southwestern Office of Business and Safety Continuity.

RNA isolations: Virus-infected cells were lysed in 300 μ L of TRI reagent 24 h post-infection. Viral RNA was isolated using Direct-zol RNA Miniprep kits (ZymoResearch, #R2053) according to manufacturer's protocol. Total RNA was eluted in 50 μ L of DNase/RNase free water.

SARS-CoV-2 positive control: SARS-CoV-2 N gene was amplified from a synthesized N gene fragment (IDT) with primers that introduced a T7 promoter sequence on the 5' end (IDT) (Table S2). PCR product was purified using Qiagen PCR Purification Kit (Qiagen). In vitro transcription was performed using T7 RiboMAX Express Large-Scale RNA Production System following manufacturers protocol (Promega). RNA was quantitated by nanodrop on DS-11 FX and by a fluorometer assay using the DeNovix RNA Assay (DeNovix). In-vitro transcribed RNA was used to generate a standard curve for qPCR from a 10-fold dilution series starting at 5×10^{10} copies of RNA.

RT-qPCR: A 25 μ L reaction contained 5 μ L RNA, 12.5 μ L of 2x reaction buffer (containing 0.4 mM of each dNTP and 6 mM $MgSO_4$), 0.5 μ L of a 2.5 μ M ROX Reference Dye solution, 0.5 μ L SuperScript III RT/Platinum Taq Mix (Invitrogen) and 1.8 μ L Primer/Probe mix (6.7 μ M each primer, 1.7 μ M probe, giving a final concentration of 500 nM each primer, 125 nM probe). SARS-CoV-2 primers and probe were designed as recommended by the Center for Disease Control (<https://www.cdc.gov/coronavirus/2019-ncov/lab/rt-pcr-panel-primer-probes.html>). GAPDH primers and probe were designed as published [76] (Table S2). All oligonucleotides were synthesized by LGC Biosearch Technologies. RT was performed at 50 °C for 5 min, followed by inactivation at 95 °C for 2 min, and 40 cycles of PCR (95 °C for 3 s, 60 °C for 30 s) on an ABI 7500 Fast thermocycler (Applied Biosystems).

Cell viability and cell toxicity assays: VeroE6 cells seeded at 12,000 cells per well in 96-well plates were incubated in the presence of each compound or DMSO as control diluted in MEM/10% FBS for 24 h. To quantify cell lysis, 50 microliters of cell supernatant was assayed for lactate dehydrogenase (LDH) release using the CytoTox 96 (Promega) assay according to manufacturer's instructions. To measure viable cells, the remaining media was aspirated from each well and replaced with 50 microliters of CellTiter-Glo (Promega) reagent diluted 1:1 with MEM/10% FBS, and incubated 10 min. Luminescence was measured for 30 microliters of each sample in a white-walled 96-well plate using a Berthold XS3 LB 960 luminometer.

Immunofluorescence: Cells were fixed with 3.7% formaldehyde in water. Cells were washed with PBS, then permeabilized with 0.2% Triton-X 100. Cells were blocked with 5% goat serum/PBS for at least 30 min. Primary antibody (J2, SciCons) was added in blocking solution and incubated for 1 h. Cells were washed 3x with PBS, after which secondary antibody (Goat-anti-mouse AlexaFluor 488, Invitrogen), was added in 5% BSA/PBS and incubated for 30 min. Cells were washed 3x with PBS, and then mounted using Vectashield Antifade Mounting Reagent with DAPI (VectorLabs). Imaging was performed on a Zeiss Observer Z.1. Images were processed in ImageJ.

Mpro protein cloning, expression, and purification: The gene for COVID-19 Mpro was cloned according to the published literature [51]. Briefly, the gene was constructed with N terminal GST tag followed by Mpro protease recognition site, Mpro protein, 3 C protease recognition site and 6xHis tag. Target protein was expressed in cultures grown in autoinduction media at 18 °C overnight [77]. The culture was harvested and sonicated in lysis buffer (50 mM Tris (pH8.0), 300 mM NaCl, 1 mM DTT and supplemented with protease inhibitors). The lysate was centrifuged, the supernatant was loaded onto a Ni-NTA affinity column (Qiagen) and the beads were washed with wash buffer (20 mM Tris (pH8.0), 300 mM NaCl, 1 mM DTT and 20 mM Imidazole (pH 8.0)) and eluted with elution buffer (20 mM Tris (pH 8.0), 150 mM NaCl, 1 mM DTT and 250 mM Imidazole (pH 8.0)). The eluate was digested by 3 C protease at 4 °C overnight and then further purified by ion exchange chromatography followed by gel filtration chromatography. The peak fractions were collected and concentrated to about 5 mg/mL with the

gel filtration buffer (20 mM Tris (pH8.0), 150 mM NaCl, 1 mM DTT and 1 mM EDTA).

Mpro enzymatic activity and inhibition assays: Mpro enzymatic activity assays were executed, as previously described with minor modifications [78]. In brief, the SARS-CoV-2 M^{pro} activity was measured by incubation of 50 μ M of the selected compounds along with 0.2 μ M SARS-CoV-2 M^{pro} and 1 mM DTT for 90 mins and 12 h, followed by 20 μ M Mpro substrate, DABCYL-KTSAVLQSGFRKME-EDANS (BPS Bioscience, San Diego, CA, U.S.), using wavelengths of 360 nm and 460 nm for excitation and emission, respectively. Fluorescence intensity was monitored with microplate reader. All experiments were performed in triplicate.

Next, we screened the Mpro activity for entacapone, dronedarone, and mebendazole at 10-dose levels (0.04 – 50 μ M). IC50s were elucidated using GraphPad Prism. All experiments were performed in duplicate.

Intact protein analysis in the presence of the compounds: Intact protein analysis in the presence of the compounds: Briefly, 12.5 μ g of SARS-Cov-2 Mpro was dissolved in 250 μ L of buffer (10 mM Tris-HCl pH 7.5 buffer containing 0.1 mM EDTA along with 2 μ L of 0.5 M DTT to 1 mL assay buffer), containing drug (ratio of 1:100), as previously described [11,79]. Liquid chromatography–mass spectrometry analyses were performed in positive-ion mode with a Sciex X500B quadrupole-time-of-flight mass spectrometer coupled with an Agilent 1290 Infinity II HPLC. Samples were injected onto a trap column packed with POROS 20 R1 reversed-phase beads and desalted for 4 min with buffer A at 300 μ L/min, then eluted onto a POROS R1 reverse-phase column (2.1 \times 30 mm, 20 μ m particle size, 4000 Å pore size) with a gradient from 0% to 55% B in 18 min, 55–80% B in 0.1 min, and held at 80% B for 4 min, as a flow rate of 300 μ L/min. Buffer A contained 0.1% formic acid in water and buffer B contained 0.1% formic acid in acetonitrile. The mass spectrometer was controlled by Sciex OS v.1.6.1 using the following settings: Ion source gas 130 psi, ion source gas 230 psi, curtain gas 35, CAD gas 7, temperature 300 °C, spray voltage 5500 V, declustering potential 80 V, collision energy 10 V. Data was acquired from 400 to 2000 Da with a 0.5 s accumulation time and 4-time bins summed. The acquired mass spectra for the proteins of interest were deconvoluted using BioPharmaView v. 3.0.1 software (Sciex) to obtain the molecular weights. The peak threshold was set to $\geq 5\%$, reconstruction processing was set to 10 iterations with a signal-to-noise threshold of ≥ 5 and a resolution of 20000.

Metabolomic analysis for atovaquone-treated Vero-E6 cells: For metabolomic studies, 10 cm culture dish of VeroE6 cells at 80% confluence were treated for 24 h with the indicated doses of atovaquone in regular culture medium. DMSO was used as vehicle control. After treatment, cells were washed with ice-cold PBS and scrapped out in 1 mL ice-cold 80% methanol. After three freeze-thaw cycles, cell debris was pelleted by centrifugation and metabolite-containing supernatant was evaporated using a SpeedVac concentrator (ThermoSavant, NY). Finally, metabolites were reconstituted in 0.03% formic acid. All metabolomics analyses were performed as the Metabolomics Core at CRI/UTSW. Targeted metabolite profiling of purine and pyrimidine pathways was performed, as previously described [80]. Untargeted metabolomics was performed by reverse-phase chromatography on a 1290 UHPLC liquid chromatography (LC) system interfaced to a high-resolution mass spectrometry (HRMS) 6550 iFunnel Q-TOF mass spectrometer (MS) (Agilent Technologies, CA). The MS was operated in both positive and negative (ESI+ and ESI-) modes. Analytes were separated on an Acquity UPLC® HSS T3 column (1.8 μ m, 2.1 \times 150 mm, Waters, MA). The column was kept at room temperature. Mobile phase A composition was 0.1% formic acid in water and mobile phase B composition was 0.1% formic acid in 100% ACN. The LC gradient was 0 min: 1% B; 5 min: 5% B; 15 min: 99% B; 23 min: 99% B; 24 min: 1% B; 25 min: 1% B. The flow rate was 250 μ L min⁻¹. The sample injection volume was 5 μ L. ESI source conditions were set as follows: dry gas temperature 225 °C and flow 18 L min⁻¹, fragmentor voltage 175 V, sheath gas temperature

350 °C and flow 12 L min⁻¹, nozzle voltage 500 V, and capillary voltage + 3500 V in positive mode and – 3500 V in negative. The instrument was set to acquire over the full *m/z* range of 40–1700 in both modes, with the MS acquisition rate of 1 spectrum s⁻¹ in profile format. Raw data files (.d) were processed using Profinder B.08.00 SP3 software (Agilent Technologies, CA) with an in-house database containing retention time and accurate mass information on 600 standards from Mass Spectrometry Metabolite Library (IROA Technologies, MA) which was created under the same analysis conditions. The in-house database matching parameters were: mass tolerance 10 ppm; retention time tolerance 0.5 min. Peak integration result was manually curated in Profinder for improved consistency and exported as a spreadsheet (.csv).

Western blotting method:

Cell extracts were collected and lysed in RIPA buffer with the addition of complete protease inhibitor cocktail (Roche). Protein concentration was quantified using Pierce BCA protein assay kit (Pierce Biotechnology), with three technical replicates. After separation via SDS-PAGE, proteins were transferred to nitrocellulose membranes (Bio-Rad), blocked in 5% skim milk/TBS and incubated with appropriate primary antibodies: NT5E/CD73 (Novus Biologicals, NBP1–85740; 1:500), GAPDH (EMD Millipore, AB2302; 1:5,000). Horseradish peroxidase-conjugated peroxidase anti-rabbit and anti-chicken (Jackson ImmunoResearch, 111–035–144, 703–035–155, 1:25000–1:50,000) were used as secondary antibodies. The membranes were explored using Licor Odyssey Fc system and quantified by Image Studio Lite v.5.2 software.

Phospholipidosis quantification for atovaquone and mebendazole-treated Vero E6 cells:

Vero E6 cells were treated with atovaquone (1–10 μM), mebendazole (1–10 μM), or DMSO as vehicle for 24 h in presence of 7.5 μM NBD-PE (ThermoFisher, ref. N360). The final DMSO concentration was 0.2%. [56]. Before imaging, the cells were stained for 20 min at 37 °C, 5% CO₂ with a solution containing Hoechst-33342 (ThermoFisher, ref. 62249) (10 μg/mL), and CellTracker Orange CMRA (ThermoFisher, C34551) (5 μM) in complete culture medium for visualizing the cytoplasm of the cells. Cells were washed once with pre-warmed HBSS + / +. Images were taken on a Nikon A1R confocal microscope equipped with a 20x objective for Hoechst-33342 (405 nm laser excitation, 450/50 filter cube), NBD-PE (488 nm laser excitation, 525/50 filter cube), and CellTracker Orange (561 nm excitation, 595/50 filter cube). The images were analyzed using CellProfiler [81]. Briefly, the nuclei were detected using the Hoechst dye and the cytoplasm for nuclei was detected based on the red staining. Then, total fluorescence intensity per cell for NBD-PE was quantified. The experiment was performed in triplicates with, at least, 200 cells analyzed per replicate.

Atovaquone PK study: All the related mouse experiments follow the recommendations in the ARRIVE guidelines [82] and were conducted in accordance with protocols approved by the Institutional Animal Care and Use Committee (IACUC) of the University of Texas Southwestern Medical Center (UTSW) and complied with the relevant ethical regulations regarding animal research. Mice were housed in a 12:12 h light: dark cycle in a temperature-controlled room in the Animal Research Center of the UTSW, with free access to water and food. Female 6-weeks old CD1 mice (Charles River) were dosed PO qd x 7 at 20 mg/kg atovaquone. Drug was clinical grade Mepron (750 mg/5 mL) diluted with 0.5% carboxymethylcellulose/0.5% Kolliphor EL/1% benzyl alcohol in dH₂O to 2 mg/mL. Dose volume was 10 mL/kg. Blood was collected via the submandibular route at various times post final dose and then animals were administered an inhalation overdose of CO₂. The chest cavity was opened, and their trachea was exposed and supported by a curved forcep. A small incision was made to allow passage of an 18 g lavage catheter connected to a 3-way stockcock with 2 5 mL syringes. The catheter was inserted and ~0.5 mL PBS injected 4 times with collection of bronchial lavages (BAL) fluid into the second syringe after each instillation. After the full volume was collected, the BAL in the output syringe was expelled into a fresh tube. The BAL was centrifuged at 9600

x g for 5 min to pellet cells and the supernatant and plasma were analyzed for compound by LC-MS/MS as described below. The urea content of both, also determined by LC-MS/MS, was used to normalize the BAL fluid content to determine the epithelial lining fluid (ELF) concentration. Plasma was diluted with commercial blank mouse plasma with EDTA. Time 0 was diluted at a 1:1 ratio. The 15- and 30-minute time points were diluted at a 1:10 dilution. The remaining time points were diluted at a 1:50 dilution. Standards and controls were prepared using standard stock solutions of atovaquone made in DMSO spiked into commercial blank mouse plasma collected with K2EDTA anticoagulant. BAL samples were run undiluted. Standards and controls were prepared using standard stocks in blank BAL. To all samples, 10 μL of internal standard (atovaquone-d4) diluted in 30 mM NH₄ Acetate was added and samples vortexed. 400 μL of ethyl acetate was added to each sample. Tubes were vortexed for 30 s, incubated at room temperature (RT) for 5 min and spun for 5 min at 16,100 x g. Supernatant was transferred to a second tube. To the first tube, 400 μL of ethyl acetate was added. Tubes were vortexed for 15 sec, incubated at RT for 5 min and spun for 5 min at 16,100 x g. Supernatant was removed and added to the tube containing supernatant previously collected. Samples were dried down under vacuum and then resuspended in 100 μL of 20:80 dH₂O: acetonitrile, 5 mM NH₄ Acetate. Samples were vortexed for 15 s, sonicated for 3 min and spun for 5 min at 16,100 x g. Supernatant was transferred to an HPLC vial and analyzed on a Sciex 4000QTRAP coupled to a Shimadzu Prominence LC using a fit-for-purpose method. Atovaquone was detected in negative multiple reaction monitoring (MRM) mode using the following transitions: 365.096–337.0 (quantitation ion), 365.096–170.8 (qualifier ion). The internal standard (IS), Atovaquone-d4, was detected using the 369.1–341.0 transition. An isocratic flow of 0.2 mL/min 2 mM NH₄ acetate with 0.8 mL/min of acetonitrile on an Agilent C18 XDB column (5-micron, 50 × 4.6 mm) was used for chromatography. Atovaquone and Atovaquone-d4 showed a retention time of 1.73 min using this method. Concentrations were determined by comparison to a 9-point standard curve. Greater than 75% of standards and 100% of quality control (QC) samples were within 15% of nominal upon back-calculation. The limit of detection (LOD) was defined to be three-fold above the signal observed in blank plasma and the limit of quantitation (LOQ) was defined as the lowest point on the standard curve above the limit of detection and within 20% of nominal. The LOQ was 1 ng/mL for both matrices. Recovery of analyte at low, medium, and high concentrations was > 90% for plasma and BAL.

Epithelial Lining Fluid (ELF) concentrations were determined using urea normalization with the following calculation after correction for free atovaquone levels in BAL.

$V_{\text{ELF}} = V_{\text{BAL}} \times \text{Urea}_{\text{BAL}} / \text{Urea}_{\text{plasma}}$, where V_{BAL} is the volume of aspired BAL fluid.

The concentration of atovaquone in ELF (Atovaquone_{ELF}) was determined from the equation.

$$\text{Atovaquone}_{\text{ELF}} = \text{Atovaquone}_{\text{BAL}} \times V_{\text{BAL}} / V_{\text{ELF}}$$

Urea levels were determined by LC-MS/MS using a Sciex 6500 + QTRAP coupled to a Shimadzu NexeraX2 LC. To 100 μL sample, 30 μL of an internal standard solution containing 10 μg/mL ¹³C, ¹⁵N-urea and ¹⁵N urea was added. 150 μL of 2 M NaCO₃ was added and the solution vortexed for 2 min 900 μL acetonitrile was added and the solution was pipetted 20 times up and down to mix. The solution was centrifuged for 10 min at 16,100 x g 4 °C. 600 μL of the upper organic layer was transferred to a new tube and dried down under vacuum with mild heat. The solution was resuspended in 100 μL 50:50 acetonitrile: dH₂O and evaluated by LC-MS/MS. Urea was detected in positive multiple reaction monitoring (MRM) mode using the following transition: 61.0–44.0. ¹⁵N-Urea was detected as the 63.0–45.0 transition and ¹³C¹⁵N -Urea was detected as 64.0–46. A gradient flow of 20 mM NH₃ formate (Buffer A) and Acetonitrile (Buffer B) was used with a Phenomenex Luna 3-micron

HILIC column (100 × 4.6 mm, 200 Å): 0–1.5 min gradient from 97% B to 60% B, 1.5–2.0 min gradient to 60% B, 2.0–4.2 min gradient to 97% B, 4.2–5.0 min 97% B. Concentrations were determined by comparison to an 8 or 10-point standard curve prepared by spiking diluted mouse plasma or BAL with urea standards made in DMSO. Greater than 75% of standards and QCs were within 15% of nominal upon back calculation. The LOQ for plasma was 10 µg/mL and for BAL it was 0.1 µg/mL. Free drug was determined by multiplying the total drug concentration by the free fraction for atovaquone in each matrix as determined by rapid equilibrium dialysis (see below). Noncompartmental PK parameters were determined with sparse sampling using WinNonlin (Pharsight).

Mebendazole PK study: All the related mouse experiments follow the recommendations in the ARRIVE guidelines [82] and were conducted in accordance with protocols approved by the Institutional Animal Care and Use Committee (IACUC) of the University of Texas Southwestern Medical Center (UTSW) and complied with the relevant ethical regulations regarding animal research. Mice were housed in a 12:12 h light:dark cycle in a temperature-controlled room in the Animal Research Center of the UTSW, with free access to water and food. Female 6-weeks old CD1 mice (Charles River) were dosed PO qd x 7 at 20 mg/kg with mebendazole (Sigma). Drug was resuspended in DMSO such that the final concentration of DMSO was 10% and diluted with 0.5% carboxymethylcellulose/0.5% Kolliphor EL/1% benzyl alcohol in dH₂O to 2 mg/mL. Dose volume was 10 mL/kg. Collection of blood and BAL were as described for atovaquone. Plasma was diluted with commercial blank mouse plasma with EDTA. Time 0 was diluted at a 1:1 ratio. The 15-minute timepoint was diluted at a 1:5 dilution. 30-, 90-, and 360-timepoints were diluted at 1:10. 180- timepoint was diluted at 1:20. 720-timepoint was diluted at 1:2. The 1440-timepoint was run undiluted. Each sample had a final volume of 50 µL. Standards and controls were prepared using standard stocks and blank commercial plasma for a total volume of 50 µL. 100 µL of Acetonitrile crash (50 ng/mL mebendazole-d3, 0.1% formic acid final) was added to each sample. Samples were vortexed for 15 seconds, incubated at room temperature for 10 min and spun for 5 min at 16,100xg twice. Supernatant was analyzed by LC-MS/MS using a Sciex 4000QTRAP coupled to a Shimadzu Prominence LC. Mebendazole was detected in positive multiple reaction monitoring (MRM) mode using the following transitions: 296.145–264.014 (quantifier ion), 296.145–105.053 (qualifier ion). The IS mebendazole-d3 was detected as the 299.19–105.1 transition. An isocratic flow of 0.2 mL/min 0.1% formic acid in dH₂O (Buffer A) and 0.8 mL/min 0.1% formic acid in Acetonitrile (Buffer B) was used with an Agilent C18 XDB column (5-micron, 50 × 4.6 mm). Mebendazole and mebendazole-d3 showed a retention time of 2.42 min with this method. Concentrations were determined by comparison to an 8–10-point standard curve prepared by spiking diluted mouse plasma or BAL with mebendazole standards made in DMSO. Greater than 75% of standards and QCs were within 15% of nominal upon back calculation. The LOQ for plasma and BAL was 1 ng/mL. Analysis of both matrices was as described for atovaquone.

Protein Binding: Binding of compounds in matrix was determined by rapid equilibrium dialysis. Briefly compounds were spiked at concentrations indicated into diluted mouse or human plasma (20x), straight BAL or tissue culture media containing 10% FBS. Samples (200 µL) in duplicate or triplicate were placed in the red side chamber of a Pierce RED device and 350 µL of PBS added to the white chamber. Plates were sealed and rocked gently at 37 °C for 4–6 hrs. Mebendazole binding was done in a 5% CO₂ atmosphere. At the end of the incubation, aliquots were removed from the PBS and then matrix chamber and mixed with an equal volume of matrix or PBS respectively. Samples were then processed and analyzed by LC-MS/MS as described above for PK samples. Stability of each compound in all matrices was assessed at the same time by incubating each compound in matrix for the same period and was always > 90%. All concentrations are approximated by peak area ratio of analytes/IS in the LCMS. Binding was determined according to the following calculation

$$\%PPB = \frac{C_R - C_W}{C_R} \times 100\%$$

Where C_R is total drug concentration in plasma in red chamber, C_W is free drug concentration in white chamber. Dilution of matrix was accounted for as follows: Undiluted $f_u = \frac{1/D}{\left(\frac{1}{f_{u2}} - 1\right) + 1/D}$.

Where D is the dilution factor and f_{u2} is the fraction unbound in the diluted matrix [83].

Conflict of interest statement

Mahmoud Salama Ahmed holds faculty position at Texas Tech University Health Sciences Center and adjunct assistant professor at UT Southwestern Medical Center.

CRediT authorship contribution statement

MSA, JWS, and HAS were responsible for conceptualization, investigation, methodology, supervision, and writing the manuscript. holds faculty position at Texas Tech University Health Sciences Center and adjunct assistant professor at UT Southwestern Medical Center. MSA, ABF, INB, PW carried out the experiments for molecular modeling, target identification, viral replication, and Mpro assays. RJD supervised the whole metabolomic studies. IMM, NUN, FO, SYK, and AS carried out metabolomic assays and analyzed the data. JLE, MBK, WF, MBM, and KM carried out the antiviral assays and analyzed the data. NSW carried out PK studies. ST coordinated the animal studies.

Data Availability

The datasets used and/or analyzed during the current study available from the corresponding author on reasonable request.

Appendix A. Supporting information

Supplementary data associated with this article can be found in the online version at [doi:10.1016/j.biopha.2023.114614](https://doi.org/10.1016/j.biopha.2023.114614).

References

- [1] Y.S. Malik, et al., Emerging novel coronavirus (2019-nCoV)-current scenario, evolutionary perspective based on genome analysis and recent developments, *Vet. Q* 40 (1) (2020) 68–76.
- [2] F. Wu, et al., A new coronavirus associated with human respiratory disease in China, *Nature* 579 (7798) (2020) 265–269.
- [3] P. Zhou, et al., A pneumonia outbreak associated with a new coronavirus of probable bat origin, *Nature* 579 (7798) (2020) 270–273.
- [4] M. Marzi, et al., Paxlovid: mechanism of action, synthesis, and in silico study, *Biomed. Res Int* 2022 (2022), 7341493.
- [5] J. Hammond, et al., Oral nirmatrelvir for high-risk, nonhospitalized adults with covid-19, *N. Engl. J. Med.* 386 (15) (2022) 1397–1408.
- [6] M. Kozlov, COVID drug Paxlovid was hailed as a game-changer. What happened? *Nature* 613 (7943) (2023) 224–225.
- [7] J.A. Malik, et al., The SARS-CoV-2 mutations versus vaccine effectiveness: new opportunities to new challenges, *J Infect. Public Health* 15 (2) (2022) 228–240.
- [8] J.Y. Noh, H.W. Jeong, E.-C. Shin, SARS-CoV-2 mutations, vaccines, and immunity: implication of variants of concern, *Signal Transduct. Target. Ther.* 6 (1) (2021) 203.
- [9] D.E. Gordon, et al., A SARS-CoV-2 protein interaction map reveals targets for drug repurposing, *Nature* 583 (7816) (2020) 459–468.
- [10] D.E. Gordon, et al., Comparative host-coronavirus protein interaction networks reveal pan-viral disease mechanisms, *Science* 370 (6521) (2020) eabe9403.
- [11] Z. Jin, et al., Structure of Mpro from SARS-CoV-2 and discovery of its inhibitors, *Nature* 582 (7811) (2020) 289–293.
- [12] W. Rut, et al., SARS-CoV-2 Mpro inhibitors and activity-based probes for patient-sample imaging, *Nat. Chem. Biol.* 17 (2) (2021) 222–228.
- [13] N. Drayman, et al., Masitinib is a broad coronavirus 3CL inhibitor that blocks replication of SARS-CoV-2, *Science* (2021) eabg5827.
- [14] M.D. Sacco, et al., Structure and inhibition of the SARS-CoV-2 main protease reveal strategy for developing dual inhibitors against Mpro and cathepsin L, *Sci. Adv.* 6 (50) (2020) eabe0751.

- [15] J. Qiao, et al., SARS-CoV-2 Mpro inhibitors with antiviral activity in a transgenic mouse model, *Science* 371 (6536) (2021) 1374–1378.
- [16] A. Frediansyah, et al., Remdesivir and its antiviral activity against COVID-19: a systematic review, *Clin. Epidemiol. Glob. Health* 9 (2021) 123–127.
- [17] S.J.F. Kaptein, et al., Favipiravir at high doses has potent antiviral activity in SARS-CoV-2-infected hamsters, whereas hydroxychloroquine lacks activity, *Proc. Natl. Acad. Sci.* 117 (43) (2020) 26955–26965.
- [18] H. Samaee, et al., Tocilizumab for treatment patients with COVID-19: recommended medication for novel disease, *Int Immunopharmacol.* 89 (Pt A) (2020), 107018.
- [19] B. Fu, X. Xu, H. Wei, Why tocilizumab could be an effective treatment for severe COVID-19? *J. Transl. Med.* 18 (1) (2020) 164.
- [20] Baricitinib in patients admitted to hospital with COVID-19 (RECOVERY): a randomised, controlled, open-label, platform trial and updated meta-analysis, *Lancet* 400 (10349) (2022) 359–368.
- [21] V. Selvaraj, et al., Baricitinib in hospitalised patients with COVID-19: a meta-analysis of randomised controlled trials, *eClinicalMedicine* 49 (2022), 101489.
- [22] M. Hoffmann, et al., SARS-CoV-2 cell entry depends on ACE2 and TMPRSS2 and is blocked by a clinically proven protease inhibitor, *Cell* 181 (2) (2020) 271–280, e8.
- [23] D. Wrapp, et al., Cryo-EM structure of the 2019-nCoV spike in the prefusion conformation, *Science* 367 (6483) (2020) 1260–1263.
- [24] R. Yan, et al., Structural basis for the recognition of SARS-CoV-2 by full-length human ACE2, *Science* 367 (6485) (2020) 1444–1448.
- [25] M. Hoffmann, H. Kleine-Weber, S. Pohlmann, A multibasic cleavage site in the spike protein of SARS-CoV-2 is essential for infection of human lung cells, *Mol. Cell* (2020).
- [26] M. Hoffmann, et al., SARS-CoV-2 cell entry depends on ACE2 and TMPRSS2 and is blocked by a clinically proven protease inhibitor, *Cell* (2020).
- [27] A.E. Gorbalenya, et al., Nidovirales: evolving the largest RNA virus genome, *Virus Res* 117 (1) (2006) 17–37.
- [28] Y.M. Baez-Santos, S.E. John St, A.D. Mesecar, The SARS-coronavirus papain-like protease: structure, function and inhibition by designed antiviral compounds, *Antivir. Res* 115 (2015) 21–38.
- [29] C. Gil, et al., COVID-19: drug targets and potential treatments, *J. Med. Chem.* 63 (21) (2020) 12359–12386.
- [30] C. Liu, et al., Research and development on therapeutic agents and vaccines for COVID-19 and related human coronavirus diseases, *ACS Central Sci.* 6 (3) (2020) 315–331.
- [31] Farag, A., et al., Identification of FDA approved drugs targeting COVID-19 virus by structure-based drug repositioning, 2020.
- [32] F. Wang, et al., Structure of main protease from human coronavirus NL63: insights for wide spectrum anti-coronavirus drug design, *Sci. Rep.* 6 (2016) 22677.
- [33] D. Li, et al., Investigation on the mechanism for the binding and drug resistance of wild type and mutations of G86 residue in HIV-1 protease complexed with Darunavir by molecular dynamic simulation and free energy calculation, *J. Mol. Model* 20 (2) (2014) 2122.
- [34] H. Kalasz, et al., Metabolism of moexipril to moexiprilat: determination of in vitro metabolism using HPLC-ES-MS, *Med Chem.* 3 (1) (2007) 101–106.
- [35] B. Pang, et al., Drug-induced histone eviction from open chromatin contributes to the chemotherapeutic effects of doxorubicin, *Nat. Commun.* 4 (2013) 1908.
- [36] C.C. Wu, et al., On the structural basis and design guidelines for type II topoisomerase-targeting anticancer drugs, *Nucleic Acids Res* 41 (22) (2013) 10630–10640.
- [37] E. Garcia-Martin, et al., Genetic determinants of metamizole metabolism modify the risk of developing anaphylaxis, *Pharm. Genom.* 25 (9) (2015) 462–464.
- [38] D. Takahashi, et al., Backbone and side-chain (1)H, (1)(5)N, and (1)(3)C resonance assignments of Norwalk virus protease, *Biomol. NMR Assign.* 6 (1) (2012) 19–21.
- [39] H. Takahashi, A. Ishida-Yamamoto, H. Iizuka, Effects of bepotastine, cetirizine, fexofenadine, and olopatadine on histamine-induced wheal-and flare-response, sedation, and psychomotor performance, *Clin. Exp. Dermatol.* 29 (5) (2004) 526–532.
- [40] W. Hughes, et al., Comparison of atovaquone (566C80) with trimethoprim-sulfamethoxazole to treat *Pneumocystis carinii* pneumonia in patients with AIDS, *N. Engl. J. Med* 328 (21) (1993) 1521–1527.
- [41] P.H. Jones, et al., Comparison of the efficacy and safety of rosuvastatin versus atorvastatin, simvastatin, and pravastatin across doses (STELLAR* Trial), *Am. J. Cardiol.* 92 (2) (2003) 152–160.
- [42] C. Wu, et al., Analysis of therapeutic targets for SARS-CoV-2 and discovery of potential drugs by computational methods, *Acta Pharm. Sin. B* (2020).
- [43] L. Zhang, et al., Crystal structure of SARS-CoV-2 main protease provides a basis for design of improved α -ketoamide inhibitors, *Science* (2020) eabb3405.
- [44] C. Scholz, et al., DOCKTITE—a highly versatile step-by-step workflow for covalent docking and virtual screening in the molecular operating environment, *J. Chem. Inf. Model* 55 (2) (2015) 398–406.
- [45] J. Harcourt, et al., Severe acute respiratory syndrome coronavirus 2 from Patient with 2019 novel coronavirus disease, United States, *Emerg. Infect. Dis.* 26 (6) (2020).
- [46] F. Touret, et al., In vitro screening of a FDA approved chemical library reveals potential inhibitors of SARS-CoV-2 replication, *bioRxiv* (2020), 2020.04.03.023846.
- [47] S. Jeon, et al., Identification of antiviral drug candidates against SARS-CoV-2 from FDA-approved drugs, *Antimicrob. Agents Chemother.* (2020).
- [48] M. Ko, et al., Comparative analysis of antiviral efficacy of FDA-approved drugs against SARS-CoV-2 in human lung cells: nafamostat is the most potent antiviral drug candidate, *bioRxiv* (2020), 2020.05.12.090035.
- [49] G.L. Nixon, et al., Antimalarial pharmacology and therapeutics of atovaquone, *J. Antimicrob. Chemother.* 68 (5) (2013) 977–985.
- [50] P. Li, et al., Characterization of plasma protein binding dissociation with online SPE-HPLC, *Sci. Rep.* 5 (1) (2015) 14866.
- [51] Z. Jin, et al., Structure of M(pro) from COVID-19 virus and discovery of its inhibitors, *Nature* (2020).
- [52] A. Cifuentes Kottkamp, et al., Atovaquone inhibits arbovirus replication through the depletion of intracellular nucleotides, *J. Virol.* 93 (11) (2019) e00389–19.
- [53] A.E. Yeo, et al., Effects of dual combinations of antifolates with atovaquone or dapsone on nucleotide levels in *Plasmodium falciparum*, *Biochem Pharm.* 53 (7) (1997) 943–950.
- [54] M.T. Cushion, et al., Effects of atovaquone and diospyrin-based drugs on the cellular ATP of *Pneumocystis carinii* f. sp. *carinii*, *Antimicrob. Agents Chemother.* 44 (3) (2000) 713–719.
- [55] T.A. Tummino, et al., Drug-induced phospholipidosis confounds drug repurposing for SARS-CoV-2, *Science* 373 (6554) (2021) 541–547.
- [56] J.K. Morelli, et al., Validation of an in vitro screen for phospholipidosis using a high-content biology platform, *Cell Biol. Toxicol.* 22 (1) (2006) 15–27.
- [57] M.M. Calderon, et al., Efavirenz but not atazanavir/ritonavir significantly reduces atovaquone concentrations in HIV-infected subjects, *Clin. Infect. Dis.* 62 (8) (2016) 1036–1042.
- [58] W. Hughes, et al., Phase I safety and pharmacokinetics study of micronized atovaquone in human immunodeficiency virus-infected infants and children. Pediatric AIDS Clinical Trials Group, *Antimicrob. Agents Chemother.* 42 (5) (1998) 1315–1318.
- [59] C. Robin, et al., Plasma concentrations of atovaquone given to immunocompromised patients to prevent *Pneumocystis jirovecii*, *J. Antimicrob. Chemother.* 72 (9) (2017) 2602–2606.
- [60] P.A. Braithwaite, et al., Clinical pharmacokinetics of high dose mebendazole in patients treated for cystic hydatid disease, *Eur. J. Clin. Pharm.* 22 (2) (1982) 161–169.
- [61] A. Bekhti, Serum concentrations of mebendazole in patients with hydatid disease, *Int J. Clin. Pharm. Ther. Toxicol.* 23 (12) (1985) 633–641.
- [62] M.K. Jain, et al., Atovaquone for treatment of COVID-19: a prospective randomized, double-blind, placebo-controlled clinical trial, *Front Pharm.* 13 (2022), 1020123.
- [63] G.V. Naccarelli, et al., Safety and efficacy of dronedarone in the treatment of atrial fibrillation/flutter, *Clin. Med. Insights Cardiol.* 5 (2011) 103–119.
- [64] R. SELDEN, T.W. SMITH, W. Findley, Ouabain pharmacokinetics in dog and man, *Circulation* 45 (6) (1972) 1176–1182.
- [65] C.R.E. Jr, et al., Sialic acid-to-urea ratio as a measure of airway surface hydration, *Am. J. Physiol. -Lung Cell. Mol. Physiol.* 312 (3) (2017) L398–L404.
- [66] F. Poutout-Belissent, S.N. Grant, J.S. Tepper, Aspiration and inspiration: using bronchoalveolar lavage for toxicity assessment, *Toxicol. Pathol.* 49 (2) (2021) 386–396.
- [67] M.M. Thapar, et al., Time-dependent pharmacokinetics and drug metabolism of atovaquone plus proguanil (Malarone) when taken as chemoprophylaxis, *Eur. J. Clin. Pharmacol.* 58 (1) (2002) 19–27.
- [68] F. Zsila, I. Fitos, Combination of chiroptical, absorption and fluorescence spectroscopic methods reveals multiple, hydrophobicity-driven human serum albumin binding of the antimalarial atovaquone and related hydroxynaphthoquinone compounds, *Org. Biomol. Chem.* 8 (21) (2010) 4905–4914.
- [69] Z. Hussein, et al., Population pharmacokinetics of atovaquone in patients with acute malaria caused by *Plasmodium falciparum*, *Clin. Pharm. Ther.* 61 (5) (1997) 518–530.
- [70] R.C. Mazarino, Targeting future pandemics, a case for de novo purine synthesis and basic research, *Front Immunol.* 12 (2021), 694300.
- [71] M. Naïm, et al., Solvated interaction energy (SIE) for scoring protein-ligand binding affinities. 1. Exploring the parameter space, *J. Chem. Inf. Model* 47 (1) (2007) 122–133.
- [72] M.S. Ahmed, et al., Identification of tetracycline combinations as EphB1 tyrosine kinase inhibitors for treatment of neuropathic pain, *Proc. Natl. Acad. Sci.* 118 (10) (2021), e2016265118.
- [73] M.S. Ahmed, et al., Biological screening of cucurbitacin inspired estrone analogs targeting mitogen-activated protein kinase (MAPK) pathway, *Chem. Biol. Drug Des.* 90 (3) (2017) 478–484.
- [74] G. Neudert, G. Klebe, DSX: a knowledge-based scoring function for the assessment of protein-ligand complexes, *J. Chem. Inf. Model* 51 (10) (2011) 2731–2745.
- [75] J.W. Schoggins, et al., Dengue reporter viruses reveal viral dynamics in interferon receptor-deficient mice and sensitivity to interferon effectors in vitro, *Proc. Natl. Acad. Sci. USA* 109 (36) (2012) 14610–14615.
- [76] K. Shirato, M. Kawase, S. Matsuyama, Middle East respiratory syndrome coronavirus infection mediated by the transmembrane serine protease TMPRSS2, *J. Virol.* 87 (23) (2013) 12552–12561.
- [77] F.W. Studier, Protein production by auto-induction in high density shaking cultures, *Protein Expr. Purif.* 41 (1) (2005) 207–234.
- [78] X. Xue, et al., Production of authentic SARS-CoV M(pro) with enhanced activity: application as a novel tag-cleavage endopeptidase for protein overproduction, *J. Mol. Biol.* 366 (3) (2007) 965–975.
- [79] E. Resnick, et al., Rapid covalent-probe discovery by electrophile-fragment screening, *J. Am. Chem. Soc.* 141 (22) (2019) 8951–8968.
- [80] A.R. Mullen, et al., Oxidation of alpha-ketoglutarate is required for reductive carboxylation in cancer cells with mitochondrial defects, *Cell Rep.* 7 (5) (2014) 1679–1690.

- [81] A.E. Carpenter, et al., CellProfiler: image analysis software for identifying and quantifying cell phenotypes, *Genome Biol.* 7 (10) (2006) R100.
- [82] N. Percie du Sert, et al., The ARRIVE guidelines 2.0: updated guidelines for reporting animal research, *PLoS Biol.* 18 (7) (2020), e3000410.
- [83] J.C. Kalvass, T.S. Maurer, Influence of nonspecific brain and plasma binding on CNS exposure: implications for rational drug discovery, *Biopharm. Drug Dispos.* 23 (8) (2002) 327–338.